



HAL
open science

Flexural wave absorption by lossy gradient elastic metasurface

Liyun Cao, Zhichun Yang, Yanlong Xu, Shi-Wang Fan, Yifan Zhu, Zhaolin Chen, Yong Li, B. Assouar

► **To cite this version:**

Liyun Cao, Zhichun Yang, Yanlong Xu, Shi-Wang Fan, Yifan Zhu, et al.. Flexural wave absorption by lossy gradient elastic metasurface. *Journal of the Mechanics and Physics of Solids*, 2020, 143, pp.104052. 10.1016/j.jmps.2020.104052 . hal-03043149

HAL Id: hal-03043149

<https://hal.science/hal-03043149>

Submitted on 7 Dec 2020

HAL is a multi-disciplinary open access archive for the deposit and dissemination of scientific research documents, whether they are published or not. The documents may come from teaching and research institutions in France or abroad, or from public or private research centers.

L'archive ouverte pluridisciplinaire **HAL**, est destinée au dépôt et à la diffusion de documents scientifiques de niveau recherche, publiés ou non, émanant des établissements d'enseignement et de recherche français ou étrangers, des laboratoires publics ou privés.

Flexural wave absorption by lossy gradient elastic metasurface

Liyun Cao^{1,2}, Zhichun Yang^{1,*}, Yanlong Xu¹, Shi-Wang Fan², Yifan Zhu², Zhaolin Chen¹, Yong Li³ and Badreddine Assouar^{2,*}

¹*School of Aeronautics, Northwestern Polytechnical University, Xi'an, 710072, China*

²*Institut Jean Lamour, CNRS, Université de Lorraine, Nancy, 54506, France*

³*Institute of Acoustics, School of Physics Science and Engineering, Tongji University, Shanghai 200092, China.*

*Corresponding author e-mails: yangzc@nwpu.edu.cn & badreddine.assouar@univ-lorraine.fr

Abstract

In this research, we systematically study the flexural waves diffraction. Based on the diffraction mechanism, we propose the concept of subwavelength lossy gradient elastic metasurface for flexural waves absorption. We theoretically reveal that the high-efficiency absorption behavior stems from maximum multireflection-enhanced absorption of 0th order diffraction, and experimentally show that robust flexural wave quasi-omnidirectional absorption in the frequency range extending approximately from 340 Hz to 1000 Hz (larger than 1.5 octaves). In addition, we propose a general approach which involves new physics of adjusting the arrangement sequence of subunits to suppress the 1st diffraction mode, to further reduce the sub-wavelength thickness of the metasurface while maintaining its high-efficiency absorption. Our designs could provide new routes to broadband vibration suppression and cancellation in low-frequency by lossy elastic metamaterials and metasurfaces.

1 **1. Introduction**

2 Vibration suppression of plate-like structures is of great significance in many
3 engineering applications, for example, preventing vibration hazards and reducing noise.
4 Since early 1950s, this research topic has been widely concerned. The conventional
5 suppression methods can be mainly divided into passive and active suppression
6 approaches. The passive suppression method (Kerwin, 1959; Sun et al., 1995;
7 Warburton, 1982), which is represented by attaching a large number of damping
8 absorbers on the plate-like structures, is difficult to fulfil the requirements of
9 lightweight and broadband features. The active suppression method (Agnes, 1994;
10 Dubay et al., 2014; Moheimani, 2003; Niederberger and Morari, 2006), which is
11 represented by applying control force through the actuator to the host structure based
12 on feedback response, has complex structure and low stability. As a new generated
13 method of vibration suppression, employing an acoustic black hole (ABH) (Krylov and
14 Winward, 2007; Ma and Cheng, 2019; McCormick and Shepherd, 2019; Pelat et al.,
15 2020; Tang et al., 2016; Warburton, 1982), which can absorb the propagating waves
16 (dominated by flexural waves) by little attached damping, promotes development of
17 lightweight suppression technique. However, the ABH has weak damping effect at low
18 frequencies and is not useful for a plethora of technological applications where the low
19 frequencies are the main source to be damped. As another new generation of vibration
20 suppression method, laying artificial periodic structures (Badreddine Assouar et al.,
21 2012; Fang et al., 2017; Oudich et al., 2010) on the plate-like structures can produce
22 bandgap to prohibit wave propagation in low-frequency. Artificial periodic structures

1 just isolate the vibration energy and do not dissipate the energy fundamentally. In
2 addition, only subunit size is sub-wavelength, and the overall size of the periodic
3 structure is still much larger than the wavelength. Recently, some vibration suppression
4 techniques based on different methods, for example an open lossy resonators in one-
5 dimensional elastic beams (Leng et al., 2019) and total reflection of propagating waves
6 (Zhu et al., 2018a), have also been proposed. However, narrowband is their common
7 characteristic. To date, it is still a great challenge to realize sub-wavelength broadband
8 vibration suppression in low-frequency. Therefore, it is necessary to explore new
9 mechanisms and approaches to break through it.

10 As one ultra-thin kind of metamaterials (Dong et al., 2020; Kweun et al., 2017;
11 Sugino et al., 2018; Zhang et al., 2020; Zhu et al., 2014a, b), acoustic metasurfaces with
12 sub-wavelength (Assouar et al., 2018; Fan et al., 2019; Li et al., 2017; Qi et al., 2017;
13 Zhu et al., 2018b) opened up new possibilities to realize extraordinary wave
14 manipulation based on the generalized Snell's law (GSL) (Yu et al., 2011). However,
15 with the development of research, it was found that the GSL will no longer be valid for
16 some new phenomena involved high order diffractions, such as incident waves beyond
17 the so-called critical angle (Liu et al., 2017a; Zhou et al., 2017) and unexpected leakage
18 waves (Cao et al., 2018b; Xie et al., 2014). For the high order diffractions, the directions
19 of diffraction channels need to be predicted by the general formulas, i.e., the diffraction
20 theorem (Larouche and Smith, 2012). Normally, several diffraction channels
21 simultaneously exist for a particular incidence, and the magnitudes of diffractions in
22 different channels will be different. Apparently, the complicated diffraction will not be

1 fully revealed by only the directions of the diffraction channels. The magnitude of each
2 order diffraction should also be explored. For revealing the comprehensive underlying
3 diffraction mechanism, the mode-coupling method (Liu and Jiang, 2018; Mei and Wu,
4 2014; Zhilin Hou, 2019) had been used to accurately solve the amplitude of each order
5 diffraction. Recently, based on these methods, the acoustic diffraction mechanism had
6 been studied systematically and some new physics related to acoustic diffraction had
7 been revealed. As typical representatives, acoustic asymmetric transmission (Li et al.,
8 2017) and acoustic absorption (Shen and Cummer, 2018; Yi Fang, 2018; Zhou et al.,
9 2017) can be obtained by high order diffraction. Anomalous transmission and reflection
10 through high order diffraction can be completely reversed by changing the integer parity
11 of the phase gradient metagratings (Fu et al., 2019).

12 Recently, although big progresses have also been subsequently achieved in the
13 field of elastic metasurfaces (Liu et al., 2017b; Xu et al., 2019b; Cao et al., 2020a; Cao
14 et al., 2018a; Chen et al., 2018; Lee et al., 2018; Li et al., 2018; Liu et al., 2017b; Park
15 et al., 2020; Qiu et al., 2019; Su et al., 2018; Tian and Yu, 2019; Xia et al., 2019; Xu et
16 al., 2019a; Yuan et al., 2020; Zhang et al., 2018; Zhu and Semperlotti, 2016), almost all
17 existing researches on elastic metasurfaces are simply related to the manipulation of the
18 wavefield based on the GSL, which is only related to 1st order diffraction. The
19 manipulation of other orders of elastic wave diffractions based on elastic metasurface
20 has not been systematically studied due to the essential difference between the elastic
21 waves and the acoustic waves; for example, more degrees of freedom and more
22 complexity of the control equation. We expect to develop an effective theoretical tool,

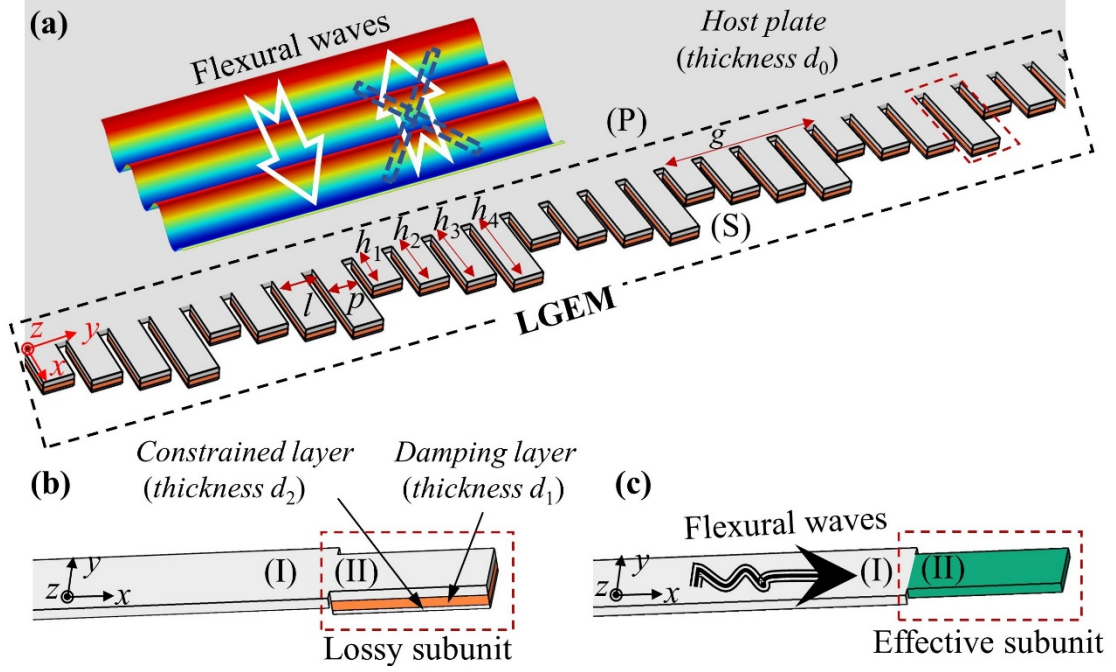
1 which is similar to the mode-coupling method in acoustics(Mei and Wu, 2014; Zhilin
2 Hou, 2019), and explore the rich physics of higher-order diffractions in the elastic
3 metasurface. Fortunately, similar methods (Willis, 2016; Srivastava, 2016), which are
4 also called mode-coupling methods for consistency, had been used in elastic waves to
5 study negative refraction of anti-plane shear waves at a plane interface between a
6 homogeneous elastic half-space and a layered periodic composite. Recently, these
7 methods (Lustig et al., 2019; Lustig and Shmuel (2018); Mokhtari et al., 2019; Mokhtari
8 et al., 2020) had been extended to study the scattering of in-plane elastic waves.
9 Although they only focus on anti-plane shear waves or in-plane waves, they provide a
10 good theoretical basis for the studies of other elastic wave patterns in different periodic
11 structures.

12 In the present study, we expand the conventional mode-coupling method to
13 systematically study the diffraction mechanism of flexural waves. Based on the
14 diffraction mechanism, we introduce the concept of lossy gradient elastic metasurface
15 (LGEM) to explore the underlying physics of flexural wave absorption. Different from
16 the inherent energy loss in acoustic waves, the small damping property of the solid
17 material makes the loss of elastic wave in the structure negligible. Therefore, we
18 introduce different lossy physical system into the elastic metasurface, which is an
19 additional constrained damping layer (i.e., a damping layer of butyl rubber and a
20 constraint layer of aluminum foil) on the subunits. For the lossy subunits, the equivalent
21 models are established to analytically predict the amplitudes and phases of reflected
22 waves. Further, we theoretically analyze the absorption performance in details. In

1 addition, we propose a general approach to reduce the sub-wavelength thickness of the
2 metasurface while maintaining its efficient absorption. Finally, both numerical
3 simulations and experiments are carried out to demonstrate the broadband and high-
4 efficiency flexural waves absorption of the LGEM in low-frequency.

5 **2. Design of the subunits of the LGEM**

6 Fig. 1(a) shows the schematic of LGEM with predesigned geometries in the host
7 plate with thickness of $d_0=3$ mm. It is composed of periodic arrays of supercells with
8 the width of g , which includes J subunits with different lengths h_j ($j=1, 2 \dots J, J=4$ in
9 Fig. 1(a)). These subunits with the width of p are separated by the slits with the width
10 of $p_0=1$ mm. In Fig. 1(b), the strip-like structure can be divided into the host plate and
11 the subunits regions, which are marked as Regions (I) and (II), respectively. It can be
12 seen that the subunit consists of three-layer composite structures. From top to bottom,
13 they are the strip-like plate, damping layer and constrained layer, with the thicknesses
14 of d_0, d_1 , and d_2 , respectively. The material of the damping layer is butyl rubber, which
15 will introduce the loss to the subunit. The material of the host plate and the constrained
16 layer, which are considered as the lossless, is aluminum with a very low damping. The
17 ultrathin constrained layer will make the energy in the plate to mainly dissipate in the
18 way of shear deformation, which can enhance the loss of the damping layer.



1

2 FIG. 1 (a) Schematic diagram of the LGEM. (b) View of a subunit composed of a strip-like plate

3 attached with damping layer and constrained layer. (c) The effective model of the lossy subunit.

4 2.1 Effective model of the lossy unit

5 First, the subunits without the damping and constrained layers are studied, i.e., d_1

6 $= d_2 = 0$. The one-dimensional governing equation for the flexural wave in the plates of

7 Regions (I) and (II) can be expressed as the following form:

$$8 \quad E_0 I_0 \frac{\partial^4 w(x,t)}{\partial x^4} + \rho_0 d_0 \frac{\partial^2 w(x,t)}{\partial t^2} = 0, \quad (1)$$

9 where E_0 is Young's modulus of the plate, ρ_0 is the density of the plate and

10 $I_0 = \frac{d_0^3}{12(1-\nu_0^2)}$ is the moment of area, in which d_0 and ν_0 are the thickness and

11 Poisson's ratio of the plate, respectively.

12 The one-dimensional governing equation of flexural waves is a fourth-order partial

13 derivative equation. The wavenumber has four solutions, i.e., two real wavenumbers

1 $\pm k_0$ and two pure imaginary wavenumbers $\pm i \cdot k_0$. The real and pure imaginary
 2 wavenumbers represent propagating and evanescent flexural waves, respectively.

3 Therefore, the general solution of displacement for the governing equation is:

$$4 \quad w_0(x, t) = \left(A_0 e^{-ik_0 x} + B_0 e^{ik_0 x} + C_0 e^{-k_0 x} + D_0 e^{k_0 x} \right) e^{i\omega t}, \quad (2)$$

5 where A_0 , B_0 , C_0 , and D_0 are complex coefficients. $A_0 e^{-ik_0 x}$ and $B_0 e^{ik_0 x}$
 6 correspond to the positive-going and negative-going propagating flexural waves,
 7 respectively. $C_0 e^{-k_0 x}$ and $D_0 e^{k_0 x}$ correspond to the positive-going and negative-
 8 going evanescent flexural waves, respectively. The real wavenumber k_0 can be

9 expressed as $k_0 = \left(\frac{\rho_0 d_0 \omega^2}{E_0 I_0} \right)^{1/4}$, in which $\omega = 2\pi f$ is the circular frequency.

10 Further, the subunits with damping and constrained layers are studied, as shown
 11 in Fig. 1(b). To simplify, the lossy subunit with a three-layer composite structure can
 12 be considered as an effective one, i.e., an isotropic plate, as shown in Fig. 1(c). The
 13 effective bending stiffness of the lossy unit can be expressed as (Ross et al., 1959):

$$14 \quad D_{\text{eff}} = (D_0 + D_{c1} + D_2) + \left[K_0 d_c^2 + K_{c1} (d_{20} - d_c)^2 + K_2 (d_{30} - d_c)^2 \right] \\
 - \left[K_{c1} \left(\frac{d_1}{12} + \frac{d_{20} - d_c}{2} \right) + K_2 (d_{30} - d_c) \right] \frac{d_{30} - d_c}{1 + g_c}. \quad (3)$$

15 Based on the effective bending stiffness, we can obtain the effective wave number k_{eff}
 16 in the lossy unit, which is corresponding to the wavenumber of the positive-going
 17 propagating mode in Eq. (1). The detailed solutions of the effective bending stiffness
 18 and effective wave number are reported in Appendix A. Due to the loss of the damping
 19 layer, the solved effective wave number has a small imaginary part. It can be expressed
 20 as $k_{\text{eff}} = k_{\text{eff}}^{\text{Re}} - i \cdot k_{\text{eff}}^{\text{Im}}$, where $k_{\text{eff}}^{\text{Re}}$ and $k_{\text{eff}}^{\text{Im}}$ are the real and imaginary parts,

1 respectively. Furthermore, the displacement of positive-going propagating flexural
 2 wave in the lossy subunit can be rewritten as $A_1 e^{-i(k_{\text{eff}}^{\text{Re}} - i k_{\text{eff}}^{\text{Im}}) x} = A_1 e^{-i k_{\text{eff}}^{\text{Re}} x} e^{-k_{\text{eff}}^{\text{Im}} x}$, where
 3 $e^{-i k_{\text{eff}}^{\text{Re}} x}$ and $e^{-k_{\text{eff}}^{\text{Im}} x}$ represent fluctuation harmonically and decay exponentially in space,
 4 respectively. Therefore, $k_{\text{eff}}^{\text{Re}}$ and $k_{\text{eff}}^{\text{Im}}$ correspond to the amplitude and phase shift of
 5 the reflection wave emanating from the lossy subunit, respectively.

6 In order to obtain the effective mechanical properties of the lossy subunit, we
 7 measure the storage modulus (the real part of the complex Young modulus) E_1^{Re} and
 8 the loss factor η of its damping layer varying with the frequency by the Dynamical
 9 Mechanical Analysis (DMA). The test set-up is shown in Fig. 2(a), and the test sample
 10 of butyl rubber is shown in the illustration in the lower left corner. The operating
 11 frequency range of our DMA is from 0 to 1000 Hz. The following investigations will
 12 be based on the measured parameters in this frequency range, which is sufficient for the
 13 following theoretical analysis of vibration absorption. The measured datum of storage
 14 modulus and loss factor are shown in Fig. 2(b). For convenience, the fitting curves of
 15 the datum are obtained, and the corresponding fitting functions can be expressed as

$$\begin{cases} E_1^{\text{Re}}(f) = 2.32 \cdot 10^{-8} \cdot f^3 - 3.65 \cdot 10^{-5} \cdot f^2 + 2.71 \cdot 10^{-2} \\ \quad \cdot f + 6.372, & (200 \text{ Hz} \leq f \leq 1000 \text{ Hz}) \\ \eta(f) = -2.71 \cdot 10^{-12} \cdot f^4 + 6.14 \cdot 10^{-9} \cdot f^3 - 4.92 \cdot 10^{-6} \\ \quad \cdot f^2 + 1.75 \cdot 10^{-3} \cdot f + 0.225, & (200 \text{ Hz} \leq f \leq 1000 \text{ Hz}) \end{cases} \quad (4)$$

17 2.2 The influence of constrained and damping layers parameters on the subunit

18 Without considering the constrained and damping layers, the phase shifts
 19 $\phi_j = 2k_0 h_j$ of the reflected waves emanating from the j^{th} subunit can be simply

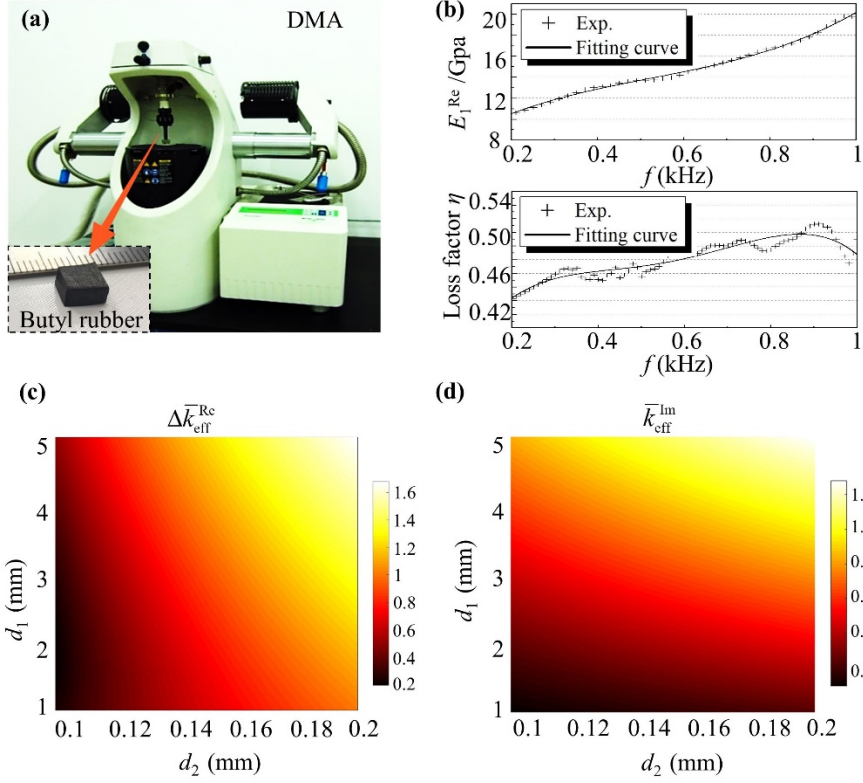
1 controlled by the lengths h_j . When these lengths of the subunits fulfil (Cao et al.,
 2 2018b)

$$3 \quad h_j = \frac{j\lambda_0}{2J} + h_0, \quad (j=1,2,\dots,J), \quad (5)$$

4 the phase shift of the reflected wave on the surface of the gradient elastic metasurface
 5 without a loss (GEM) is approximately linear, where $\lambda_0=2\pi/k_0$ and h_0 are the
 6 wavelength and additional fixed length, respectively. In this way, the reflected wave
 7 can be manipulated by the GEM based on the GSL and diffraction theorem. In these
 8 subunits, the phase shift between the two subunits of the 1st subunit and J^{th} subunit is
 9 the maximum, i.e., $\text{Max}(\phi)=2(h_J-h_1)k_0$. After introducing the constraint damping layer
 10 to the subunits, the maximum phase shift will be rewritten as $\text{Max}(\phi)_{\text{loss}}=2(h_J-h_1)k_{\text{eff}}^{\text{Re}}$.
 11 For independently defining the effect of loss and phase shift on absorption, when the
 12 difference between the phase resolution for lossless and lossy subunits is less than about
 13 $0.32\% \cdot 2\pi \approx 0.02$ rad, the phase difference caused by the constraint damping layer can
 14 be ignored. Therefore, the difference between the two maximum phase shifts needs to
 15 fulfil

$$16 \quad \Delta\phi = |\text{Max}(\phi) - \text{Max}(\phi)_{\text{loss}}| < 0.02(J-1) \text{ rad}. \quad (6)$$

17 In this way, the phase gradient designed by Eq. (5) can still be approximately linear
 18 for the lossy subunits.



1

2 FIG. 2 (a) The test set-up of Dynamical Mechanical Analysis (DMA). (b) The fitting curves for the
 3 measured storage modulus and loss factor. (c) and (d) The analytical results of $\Delta \bar{k}_{\text{eff}}^{\text{Re}}$ and $\bar{k}_{\text{eff}}^{\text{Im}}$,
 4 which give a quantitative evaluation of the dependence of the real and imaginary parts of k_{eff} on
 5 the thicknesses of the damping layer d_1 and the constrained layer d_2 , respectively.

6

According to Eqs. (5)-(6), we can get

7

$$\Delta k_{\text{eff}}^{\text{Re}} = |k_{\text{eff}}^{\text{Re}} - k_0| < \frac{0.02J}{\lambda_0}. \quad (7)$$

8

9

10

11

12

13

The central frequency in our design is 600 Hz, corresponding to a wavelength of $\lambda_0 = 221.2$ mm. Without loss of generality, the number of subunits and additional fixed length are chosen as $J = 12$ and $h_0 = \lambda_0 / 2$, respectively. In order to obtain a quantitative evaluation of the dependence of the real and imaginary parts of k_{eff} on the thicknesses of the damping layer d_1 and the constrained layer d_2 , we define the correlation coefficient as

$$\Delta \bar{k}_{\text{eff}}^{\text{Re}}(d_1, d_2) = \frac{1}{f_{\text{max}} - f_{\text{min}}} \int_{f_{\text{min}}}^{f_{\text{max}}} \Delta k_{\text{eff}}^{\text{Re}}(d_1, d_2, f) df, \quad (8)$$

$$\bar{k}_{\text{eff}}^{\text{Im}}(d_1, d_2) = \frac{1}{f_{\text{max}} - f_{\text{min}}} \int_{f_{\text{min}}}^{f_{\text{max}}} k_{\text{eff}}^{\text{Im}}(d_1, d_2, f) df, \quad (9)$$

where f_{min} and f_{max} are the frequencies of 200 Hz and 1000 Hz, respectively. The analytical results of $\Delta \bar{k}_{\text{eff}}^{\text{Re}}$ and $\bar{k}_{\text{eff}}^{\text{Im}}$ are shown in Figs. 2(c) and 2(d), respectively. Recalling Eq. (7), we can get $\Delta k_{\text{eff}}^{\text{Re}} < 0.02J / \lambda_0 \approx 1.08$ where the phase difference caused by the constraint damping layer can be ignored. Therefore, the corresponding the correlation $\Delta \bar{k}_{\text{eff}}^{\text{Re}}$ can be chosen as 0.9. According to Figs. 2(c) and 2(d), the thicknesses of the damping layer and the constrained layer is 3 mm and 0.15 mm, respectively.

2.3 The amplitude and phase shift of the subunits

For the subunits with the certain thicknesses of constrained and damping layers, $\Delta k_{\text{eff}}^{\text{Re}}$ and $k_{\text{eff}}^{\text{Im}}$ varying with frequency are shown in Fig. 3(a), respectively. It can be seen that the value of $\Delta k_{\text{eff}}^{\text{Re}}$ is less than 1.08 in the whole frequency range and $k_{\text{eff}}^{\text{Im}}$ increases with the frequency. This verifies that phase difference caused by the designed constraint damping layer can be ignored. Further, we accurately solve the amplitude and phase shift of the reflected waves emanating from the lossless and lossy subunits. The displacement w , slope φ , shear force V , bending moment M and the complex coefficients A , B , C , D for Regions (I) and (II) in Fig. 1(b) can be organized as a state vector $\mathbf{v} = \{w, \varphi, M, V\}^T$ and a coefficients vector $\mathbf{k} = \{A, B, C, D\}^T$, respectively. The positive directions of the shear force V and bending moment M are marked at the interfaces between Regions (I) and (II), as shown in the

1 illustration of Fig. 3(b). The slope φ , bending moment M and shear force V can be
 2 expressed in term of the displacement as $\varphi = w'$, $M = EIw''$, and $V = -EIw'''$,
 3 respectively, where the superscript $'$ indicates space differentiation with respect to
 4 the corresponding coordinate. The relationships between the state and coefficient
 5 vectors in Regions (I) and (II) can expressed respectively as

$$6 \quad \begin{aligned} \mathbf{v}^{(I)} &= T_1 \cdot \mathbf{k}^{(I)} \\ \mathbf{v}^{(II)} &= T_2 \cdot \mathbf{k}^{(II)} \end{aligned} \quad (10)$$

7 where T_1 and T_2 are the transformation matrix between the state and the coefficient
 8 vectors. They are given in Appendix B.

9 The boundary conditions at the interface, as shown in the illustration of Fig. 3(b),
 10 can be expressed as

$$11 \quad \begin{aligned} w_R^{(I)} &= w_L^{(II)}, \\ \varphi_R^{(I)} &= \varphi_L^{(II)}, \\ M_R^{(I)} &= \begin{cases} M_L^{(II)}, & y < y_j + |p| \\ 0, & \text{other} \end{cases} \\ V_R^{(I)} &= \begin{cases} V_L^{(II)}, & y < y_j + |p| \\ 0, & \text{other} \end{cases} \end{aligned} \quad (11)$$

12 where y_j is the position coordinate of the j^{th} subunit. We further obtain the transfer
 13 equation between the state vectors of the right end in Region (I) and the left end in
 14 Region (II) by integrating Eq. (11) with dy at the region $y < y_j + |l/2|$

$$15 \quad \mathbf{v}_L^{(II)} = \begin{bmatrix} 1 & 0 & 0 & 0 \\ 0 & 1 & 0 & 0 \\ 0 & 0 & \varepsilon & 0 \\ 0 & 0 & 0 & \varepsilon \end{bmatrix} \mathbf{v}_R^{(I)} = T_3 \mathbf{v}_R^{(I)}, \quad (12)$$

16 where l is the total width of subunit and slit, $\varepsilon = l/p$. According to Eqs. (10) and (12),
 17 we can get

$$1 \quad \mathbf{k}_L^{(II)} = T_2^{-1} T_3 T_1 \mathbf{k}_R^{(I)} = T_t \mathbf{k}_R^{(I)}. \quad (13)$$

2 It should be pointed out that when the transfer matrix of coefficients vectors T_t is an
 3 identity matrix, the impedances of Regions (I) and (II) at the interface are matched. It
 4 means that the propagating wave will not be reflected from the interface.

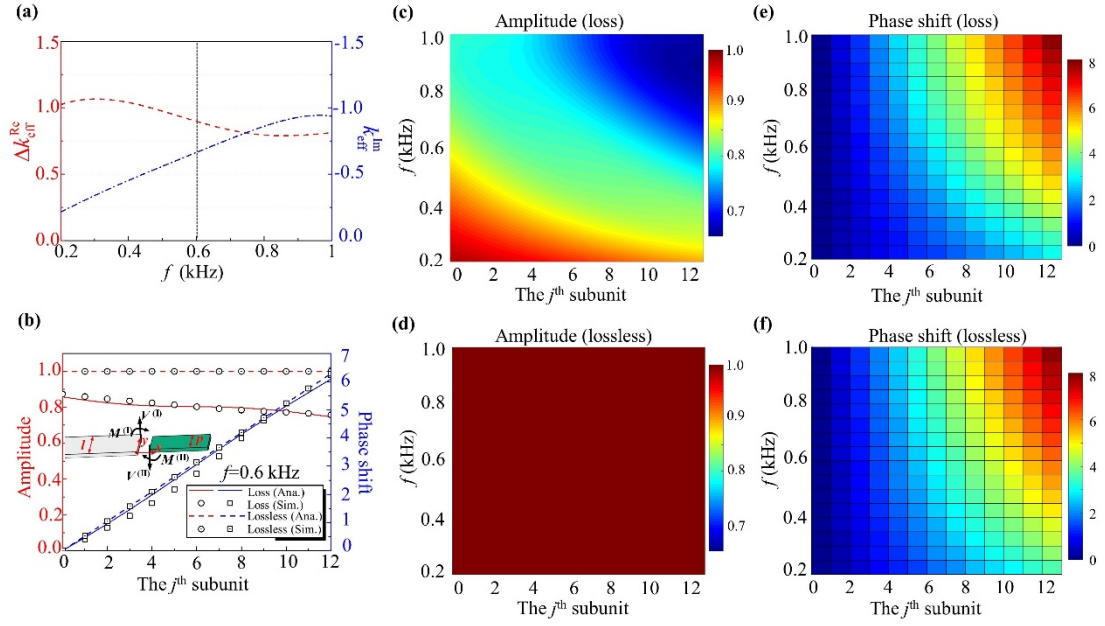
5 On the other hand, it needs to fulfil the requirement of free boundary conditions in
 6 the right boundary of Region (II), i.e., the shear force and the bending moment should
 7 be zero. It gives

$$8 \quad T_4 \mathbf{k}_L^{(II)} = 0, \quad (14)$$

9 where T_4 is the matrix for the free boundary conditions and given in Appendix B. The
 10 wave field for Region (I) can be described as $w^{(I)}(x) = e^{-ik_{b1}x} + r_b e^{ik_{b1}x} + r_b^* e^{k_{b1}x}$, where
 11 $e^{-ik_{b1}x}$ is the incident flexural wave with an amplitude of 1. r_b and r_b^* are the
 12 amplitude ratios of the reflected propagating flexural wave and reflected evanescent
 13 flexural wave in Region (I), respectively. Thus, we can get the coefficient vectors
 14 $\mathbf{k}_R^{(I)} = [1, r_b, 0, r_b^*]^T$. According to Eqs. (13) and (14), we have

$$15 \quad T_4 T_t \mathbf{k}_R^{(I)} = T_5 \mathbf{k}_R^{(I)} = 0, \quad (15)$$

16 where T_5 is the transfer matrix for the j^{th} subunit. The amplitude ratio and corresponding
 17 phase of the reflected propagating flexural wave in the far field of Region (I) can be
 18 solved by Eq. (15) (Cao et al., 2020b; Xu et al., 2019a). The phase shifts of the reflected
 19 waves for all subunits are obtained by subtracting their phase from the phase for the 1st
 20 unit. When k_{eff} and D_{eff} are equal to k_0 and D_0 , respectively, the transfer matrix T_5 of the
 21 lossy subunits will degenerate into that of the lossless subunits.



1

2 FIG. 3 (a) $\Delta k_{\text{eff}}^{\text{Re}}$ and $k_{\text{eff}}^{\text{Im}}$ varying with frequency when the thicknesses of the constrained and
 3 damping layers are 3 mm and 0.15 mm, respectively. (b) The analytical amplitudes and phase shifts
 4 of reflected waves for the lossy and lossless subunits in the central frequency of 600 Hz. The
 5 corresponding simulated results are also added. The analytical model is shown in the illustration.
 6 The phase shifts and amplitudes varying with frequency for the lossy and lossless subunits are
 7 shown in (c), (e) and (d), (f), respectively.

8 The analytical amplitudes and phase shifts of reflected waves emanating from the
 9 lossy subunits are solved in the central frequency of 600 Hz, as shown in Fig. 3(b) by
 10 red solid line and blue solid line, respectively. To evaluate the accuracy of the analytical
 11 solution, the simulated results are also depicted in Fig. 3(b). It can be seen that the
 12 simulated results are in very good agreement with the corresponding analytical results.
 13 The phase shifts of the lossy subunits are almost the same as that of the lossless subunits,
 14 while the amplitudes of the lossy subunits are reduced by about 80%. To quantify the
 15 performance of the subunits, we further examine the phase shifts and amplitudes

1 varying with the frequency for the lossy subunits (see Figs. 3(c) and 3(e)) and lossless
2 subunits (see Figs. 3(d) and 3(f)). The phase shifts of the lossy subunits are almost the
3 same as that of the lossless in the whole frequency range, while the amplitude of the
4 lossy subunit decreases with frequency. This again verifies the phase shift caused by
5 the loss in the designed subunits can be ignored. Furthermore, we can independently
6 explore the effect of loss and phase shift on flexural wave absorption.

7 **3. Analysis of flexural wave diffraction**

8 *3.1 Mode-coupling method for flexural waves*

9 The above designed subunits are arranged periodically to compose the LGEM, as
10 shown in Fig. 1(a). The reflection angles of these diffraction modes can be calculated
11 by the diffraction theorem

$$12 \quad k_{yn} = k_y^{\text{in}} + n\gamma, \quad (16)$$

13 where $k_y^{\text{in}} = k_0 \sin \theta_{\text{in}}$ and $k_{yn} = k_0 \sin \theta_r^n$ mean y -component wave vectors of the
14 incident waves and n^{th} order diffraction, respectively. θ_r^n and θ_{in} are the reflection
15 angle of the n^{th} order diffraction and the incident angle. $\gamma = \frac{2\pi}{g}$ describes the phase

16 gradient along the LGEM, and g is the width of the supercell. When $n = 1$, Eq. (16)

17 is transformed to $k_{yn} = k_y^{\text{in}} + \gamma$, yielding the well-known GSL. According to Eq. (16),

18 we can get the reflection angle of the n^{th} order diffraction by

$$19 \quad \sin \theta_r^n = \sin \theta_{\text{in}} + n \frac{\gamma}{k_0}. \quad (17)$$

20 Further, we expand the mode-coupling method to calculate the reflection amplitudes of
21 these flexural wave diffraction modes. In Fig. 1(a), the host plate and the LGEM

1 structure are divided into Region (P) and Region (S). For the sake of universality to
 2 study the vertically and obliquely incident flexural waves in the host plate, the
 3 governing equation for the flexural wave in Region (P) should be reconsidered in the
 4 two-dimension form:

$$5 \quad D_0 \left(\nabla^2 \nabla^2 + \rho_0 d_0 \frac{\partial^2}{\partial t^2} \right) w^{(P)}(x, y, t) = 0, \quad (18)$$

$$6 \quad \text{where } \nabla^2 = \frac{\partial^2}{\partial x^2} + \frac{\partial^2}{\partial y^2}.$$

7 The displacement field including all diffraction modes in Region (P) can be
 8 expressed as:

$$9 \quad w^{(P)}(x, y) = \sum_{n=0}^{\pm\infty} (\delta_{n,0} \cdot A_i e^{-ik_{y0} \cdot y} e^{-ik_{x0} \cdot x} + A_n e^{-ik_{yn} \cdot y} e^{ik_{xn} \cdot x} + B_n e^{-ik_{yn} \cdot y} e^{\hat{k}_{xn} \cdot x}), \quad (19)$$

10 where $\delta_{n,0}$ is the Kronecker delta, A_i is the amplitude of the incident wave, A_n and B_n
 11 are the reflection amplitudes of the n^{th} order propagating and n^{th} order evanescent
 12 flexural wave diffraction modes, respectively. $k_{xn} = \sqrt{k_0^2 - k_{yn}^2}$ and
 13 $\hat{k}_{xn} = -i\sqrt{-k_0^2 - k_{yn}^2}$ are x -component wave vectors of the propagation and evanescent
 14 flexural wave diffraction modes, respectively.

15 Recalling Eq. (17), when the phase gradient γ fulfils the relation of

$$16 \quad \left| n \frac{\gamma}{k_0} \right|_{n=\hat{N}} < 2, \text{ we always can find an incident angle } \theta_{\text{in}} \text{ in the range from } -90^\circ \text{ to } 90^\circ$$

17 to make the reflection angle $\theta_r^{\hat{N}}$ of the \hat{N}^{th} order diffraction exist, where \hat{N} is the
 18 maximum of all the existing orders. In other words, there will exist the propagating

19 diffraction modes of from the $-\hat{N}^{\text{th}}$ order to the \hat{N}^{th} order when the phase gradient

20 γ fulfils the relation of $|\hat{N}| < \frac{2k_0}{\gamma}$, while other order diffraction modes are evanescent.

1 The infinite summation in Eq. (19) includes only infinite propagating diffraction
 2 modes. The number of propagation modes can be determined by

$$3 \quad N=2\hat{N}+1=2 \cdot \text{roundup}(2k_0 / \gamma)-1, \quad (20)$$

4 where “roundup” is a function which rounds up to the nearest integer. Therefore, the
 5 total number of those propagating modes is controlled by the phase gradient γ . The
 6 coefficient vector of the reflection diffraction field in Region (P) can be defined as

$$7 \quad \mathbf{T}_r^P = [\mathbf{e}_1, \dots, \mathbf{e}_n, \dots, \mathbf{e}_N]^T, \text{ where } \mathbf{e}_n = [A_n, B_n].$$

8 In Region (S), since the width of the subunit is much smaller than the operating
 9 wavelength, only the fundamental mode needs to be considered. The displacement of
 10 flexural waves in the j^{th} subunit can be expressed as

$$11 \quad w_j^{(S)}(x) = a_j e^{-ik_{\text{eff}} \cdot x} + b_j e^{-k_{\text{eff}} \cdot x} + c_j e^{ik_{\text{eff}} \cdot x} + d_j e^{k_{\text{eff}} \cdot x}, \quad (21)$$

12 where a_j , b_j , c_j , and d_j are the amplitude coefficients. The coefficient vector of
 13 the fundamental mode in Region (S) can be defined as $\mathbf{T}^S = [\mathbf{k}_1, \dots, \mathbf{k}_j, \dots, \mathbf{k}_J]^T$, where
 14 $\mathbf{k}_j = [a_j, b_j, c_j, d_j]$.

15 In the direction perpendicular to the periodic waveguide plates, waveshapes
 16 related to the y -component wave vectors of the reflected diffraction modes have the
 17 orthogonal relation:

$$18 \quad \int_{-g/2}^{g/2} \psi_j \cdot \psi_n^* dy = 0, \quad (j \neq n), \quad (22)$$

19 where $\psi_n = e^{-ik_{yn} \cdot y}$. Continuity (11) and orthogonality (22) are employed and mode-
 20 coupling method is expanded to calculate these flexural wave diffraction modes. We
 21 get a linear equation set about \mathbf{T}_r^P and \mathbf{T}^S :

$$\mathbf{G}_1 \cdot \begin{pmatrix} \mathbf{T}_r^p \\ \mathbf{T}_s^p \end{pmatrix} = \mathbf{G}_2 \cdot \mathbf{T}_i^p, \quad (23)$$

where \mathbf{T}_i^p is a column vector of size $(4J + 2N)$ whose elements are all A_i , \mathbf{G}_1 and \mathbf{G}_2 are square matrices of size $(4J + 2N) \times (4J + 2N)$. The detailed derivation can be found in Appendix C. The corresponding amplitudes of diffraction modes can be calculated by solving Eq. (23). The reflection coefficient of the n^{th} order diffraction mode can be defined as

$$r_n = \frac{k_{n0} \cdot |A_n|^2}{k_{x0} \cdot |A_i|^2}, \quad (24)$$

which represents the ratio of reflected energy to incident energy for n^{th} order mode in x -axis direction. When k_{eff} and D_{eff} are equal to k_0 and D_0 , respectively, Eqs. (23) and (24) will degenerate to calculate reflection coefficient of diffraction modes for the lossless GEM.

3.2 The reflection angle and amplitude of each diffraction wave

First, without loss of generality, we begin with a lossless GEM with the phase gradient of $\gamma = k_0$. According to Eq. (20), three propagation modes can be predicted in the reflection field. The corresponding reflection angles of these modes are calculated by Eq. (17), as shown in Fig. 4(a-i). And the reflection coefficients associated with each order diffraction are obtained by Eqs. (23) and (24), as shown in Fig. 4(a-ii). The reflection coefficient associated with the 1st or -1th order mode is 1 at a relatively small incident angle, while the 0th order mode dominates at a big incident angle. After the loss is considered in the LGEM, the corresponding reflection angles and reflection coefficients of these diffraction modes are shown in Figs. 4(b-i) and 4(b-ii). It can be

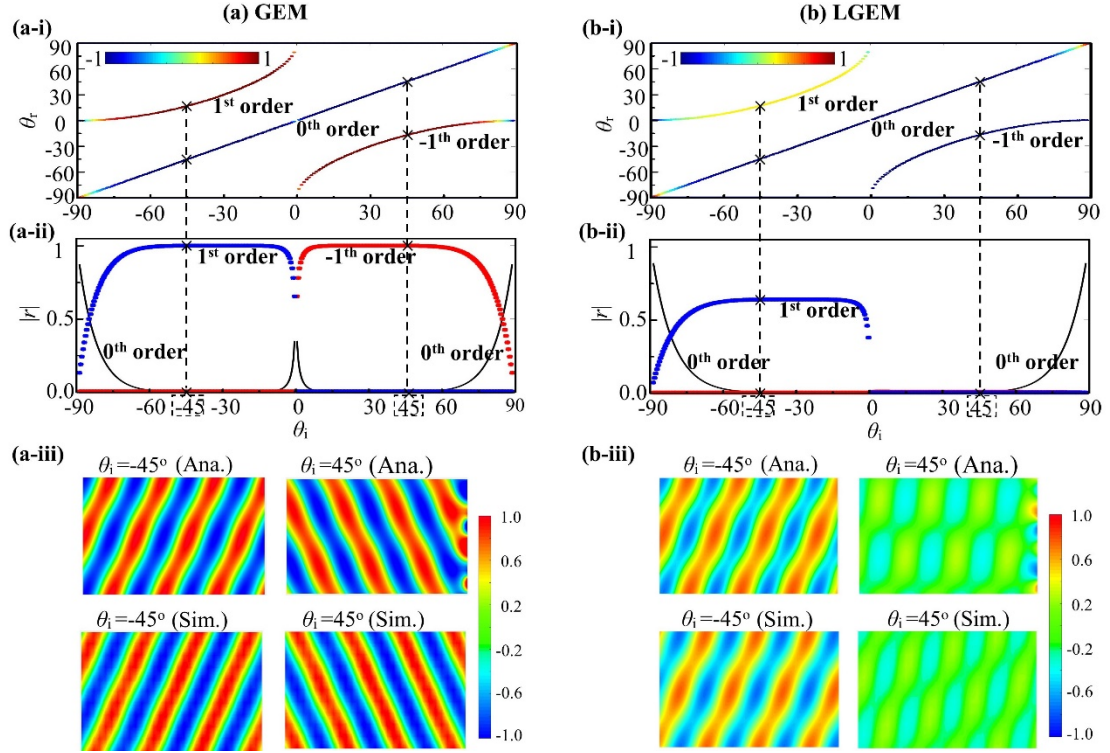
1 seen from Fig. 4(b-ii) that the total number of the propagation diffraction modes has
2 changed to 2 due to the absence of the -1th order mode.

3 For intuitively displaying the above analytic results, the incident angles of -45°
4 and 45° for the GEM and LGEM are chosen to show the full reflection fields. Based on
5 the solved complex amplitudes of three diffraction modes including propagating and
6 evanescent ones, the total full reflected wave fields in Region (P) can be solved by

$$7 \quad w_r^t(x, y) = \text{Re} \left[\sum_n (A_n e^{-ik_{ym} \cdot y} e^{ik_{xm} \cdot x} + B_n e^{-ik_{ym} \cdot y} e^{k_{xm} \cdot x}) \right]. \quad (25)$$

8 The analytical reflected wave fields for the GEM and LGEM are shown in Figs. 4(a-iii)
9 and 4(b-iii), respectively. It can be seen that the reflection amplitudes for the GEM are
10 1 with the incident angles of -45° and 45°, while the reflection amplitudes for the LGEM
11 are close to 0.8 and 0 with the incident angles of -45° and 45°, respectively. Furthermore,
12 the corresponding simulation of full wave field are performed. It can be seen from Figs.
13 4(a-iii) and 4(b-iii) that the simulation results are in good agreement with the analytical
14 ones. This confirms the accuracy of the proposed analytical method.

15 It should be pointed out that the sum of the reflection coefficients of all different
16 order modes for the lossless GEM is always 1 at different incident angles, as shown in
17 Fig. 4 (a-ii). The analytical and simulated reflection wave fields in Fig. 4 (a-iii) also
18 show that the reflection amplitudes are 1. In other words, the incident energy of flexural
19 waves is proved to be equal to the reflected energy. Therefore, there is no mode
20 conversion in the GEM structure. In addition, since it is known that the loss cannot
21 induce mode conversion, the mode conversion does not exist in the LGEM.



1
2 FIG.4 LGEM and GEM with surface phase gradient $\gamma=k_0$. (a-i) and (b-i) The corresponding
3 reflection angles of these diffraction modes for the GEM and LGEM, respectively. The color scale
4 in (a-i) and (b-i) represent the value of reflection coefficient. (a-ii) and (b-ii) The reflection
5 coefficient associated with each order diffraction mode for the GEM and LGEM, respectively. (a-
6 iii) and (b-iii) Analytical and simulated full reflection wave fields for the GEM and LGEM,
7 respectively.

8 4. Design of the quasi-omnidirectional LGEM and the internal mechanism

9 4.1 Propagation diffraction modes induced by multiple reflections

10 In order to reveal the underlying physics of the disappearance of -1^{th} order
11 diffraction mode after considering damping in Fig. 4(b-ii), we reexamine the diffraction
12 theorem of Eq. (16). The physical meaning of $n\gamma=n \cdot 2\pi / g$ in Eq. (16) is an extra
13 momentum in y direction, where the value of n corresponds to n^{th} order diffraction.
14 When $n = 1$, the extra momentum corresponds to 1^{st} order diffraction and the diffraction

1 theorem of Eq. (16) degenerates into the GSL. The total phase shift of the supercell
 2 consisting of J subunits is 2π , so the phase shifts between adjacent subunits is $2\pi/J$.
 3 It is known for the GSL that the phase shifts of these subunits are caused by one-time
 4 reflection of the incident wave in the subunit. When $n = N^* > 0$, the total phase shift
 5 of the supercell is $N^* \cdot 2\pi$, which corresponds to the N^{*th} order diffraction. The phase
 6 shifts between adjacent subunits increase to N^* times, i.e., $N^* \cdot 2\pi/J$, while the
 7 geometric size of subunits remains unchanged. The phase shifts of these subunits
 8 $N^* \cdot 2\pi/J$ need to be matched by N^* -times reflection of the incident wave in the
 9 subunit. Therefore, N^{*th} order diffraction corresponds to N^* -times reflection in the
 10 subunit.

11 Similarly, when $n = N^* \leq 0$, the total phase shift of the supercell consisting of J
 12 subunits is $N^* \cdot 2\pi$. Therefore, the phase shifts between adjacent subunits is
 13 $N^* \cdot 2\pi/J$. But the phase shift is a negative value, which doesn't fit the actual physics.
 14 Due to the periodicity of waves, the negative phase shift is equivalent to
 15 $2\pi + N^* \cdot 2\pi/J$. It needs to be matched by E -times reflection of the incident wave in
 16 the subunit. Recalling the phase shift between the adjacent subunits is $2\pi/J$ for the
 17 one-time reflection of the incident wave in the subunit. Therefore, we can get

$$18 \quad 2\pi + \frac{N^* \cdot 2\pi}{J} = E \cdot \frac{2\pi}{J}. \quad (26)$$

19 After simplification, Eq. (26) can be expressed as $E = J + N^*$. Therefore, the time of
 20 multiple reflections in the subunit corresponding to the N^{*th} order diffraction can be
 21 expressed as

$$E = \begin{cases} N^*, & N^* > 0 \\ J + N^*, & N^* \leq 0 \end{cases} \quad (27)$$

According to Eq. (27), we can calculate the times of multiply reflection in the subunit for all propagation diffraction modes in Fig. 4(a-ii). The times of multiply reflection for the -1th order, 0th order, and 1st order diffraction modes are 11, 12, and 1, respectively. On the other hand, the lower the corresponding times of multiple reflections for the existing propagation diffraction modes is, the less the resistance from the structure is. The diffraction mode with the least times of multiply reflections will dominate in all existing propagation modes. When the incident angle is the positive, existing propagation modes are the -1th order and 0th order ones. The times of multiply reflection for the -1th order one is less than that for the 0th order one. Therefore, the -1th order diffraction dominates, as shown in Fig. 4(a-ii). Similarly, when the incident angle is negative, the 1st order diffraction dominates. In Fig. 4(b-ii), when the damping is taken into account, 11-times multiply reflection for the -1th order diffraction will enhance damping dissipation of flexural waves. It leads to that the absorption of the -1th order diffraction is greater than that of the 1st order diffraction. This is the reason for the disappearance of the -1th order diffraction mode after considering damping.

4.2 Verification of multiple reflections

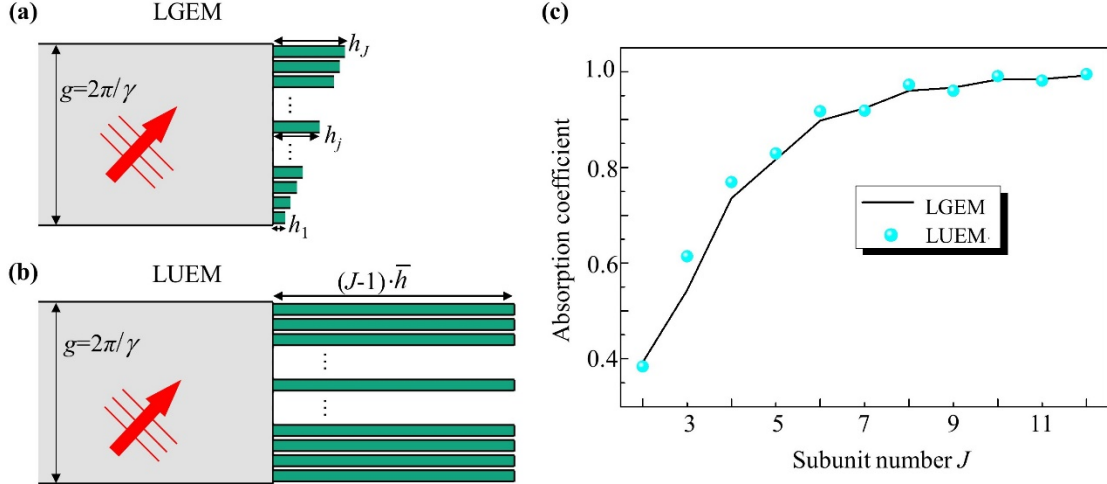
In order to verify the above multiple reflections, the case that the incident wave with the incident angle of 45° propagates into the LGEM with the phase gradient of $\gamma = k_0$ is adopted. The central frequency is 600 Hz. The model of the LGEM is shown in Fig. 5(a). The corresponding lengths of the subunits are $h_1, h_2, \dots, h_{j-1}, h_j,$

1 respectively, which can be solved by Eq. (5). According to the above analysis, the -1th
 2 order diffraction dominates in the reflection wave field, which will be absorbed by the
 3 LGEM. The absorption coefficients considering all diffraction modes can be defined as
 4 $\alpha=1-\sum_{n=0}^{\pm\infty}|r_n|$. We calculate the absorption coefficients varying with the number of
 5 subunits J in the supercell according to Eqs. (23) and (24). The results are shown in
 6 Fig. 5(c).

7 For comparison, we design another model, as shown in Fig. 5(b), in which all
 8 subunit lengths are set to the same value of \bar{h} . The model is named as the lossy
 9 uniform elastic metasurface (LUEM). The corresponding widths of the subunits and
 10 supercell are the same with the LGEM. When the uniform subunit length of LUEM
 11 fulfils $\bar{h} = \frac{1}{J} \sum_{j=1}^J h_j$, the damping area of the LUEM is the same as that of the LGEM.
 12 If the incident wave is reflected by one time in the subunit of the LGEM, the absorption
 13 coefficients for the LUEM and the LGEM will be the same. However, in the section
 14 4.1, it shows that the incident wave with the incident angle of 45° will be reflected by
 15 $J-1$ times in the LGEM due to the dominant -1th order diffraction.

16 Therefore, we increase the subunit length of the LUEM to $(J-1) \cdot \bar{h}$. In this way,
 17 we analytically calculate the absorption coefficient of the LUEM for the incident wave
 18 with the incident angle of 45° according to Eqs. (23) and (24). The results are depicted
 19 in Fig. 5(c). It can be seen that the absorption coefficient of the LUEM is exactly the
 20 same as that of the LGEM with different numbers of subunits. This result verifies that
 21 the times of multiple reflections for the -1th order diffraction is $J-1$ calculated by Eq.

1 (27).



2

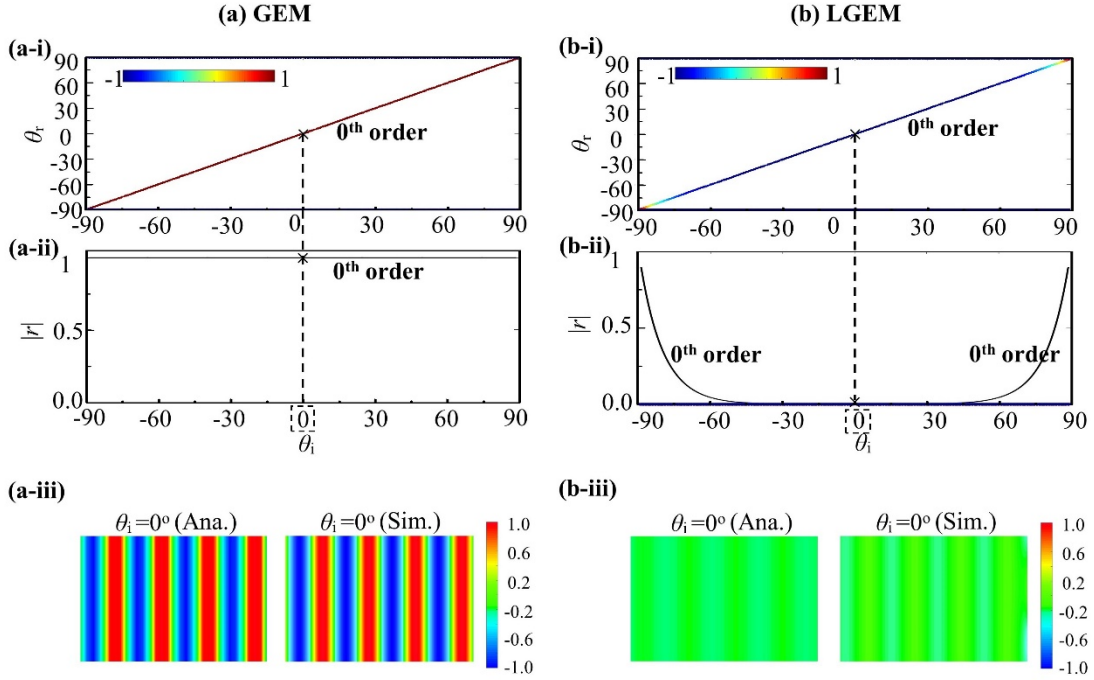
3 FIG. 5 (a) The supercell of LGEM, which is composed of J subunits. (b) The supercell of LUEM
 4 with the uniform subunit length of $(J-1)\cdot\bar{h}$. (c) The analytical absorption coefficients of the
 5 LGEM and the LUEM.

6 4.3 Quasi-omnidirectional flexural wave absorption of the LGEM

7 According to Eq. (27), we know that the number of multiple reflections for the 0th
 8 order propagation mode in the LGEM is J times, which is the highest in that for all
 9 propagation modes. According to Eq. (20), we can adjust the surface phase gradient of
 10 the LGEM ($J=12$) as $\gamma=2.1k_0$, so that there is only one propagation mode, i.e., the 0th
 11 order one, in the reflection field. In the later research, we all adopt the LGEM with the
 12 phase gradient of $\gamma=2.1k_0$. When the loss is not considered, the corresponding
 13 reflection angles and reflection coefficients of these diffraction modes are calculated
 14 analytically, as shown in Figs. 6(a-i) and 6(a-ii), respectively. It can be seen that the
 15 amplitudes of the 0th order modes are always 1 for all incident angles in Fig. 6(a-ii).

16 When the loss is considered, the reflection coefficients jump from 1 to less than
 17 0.2 for the incident angles from -75° to 75° due to the multiple reflections, as shown in

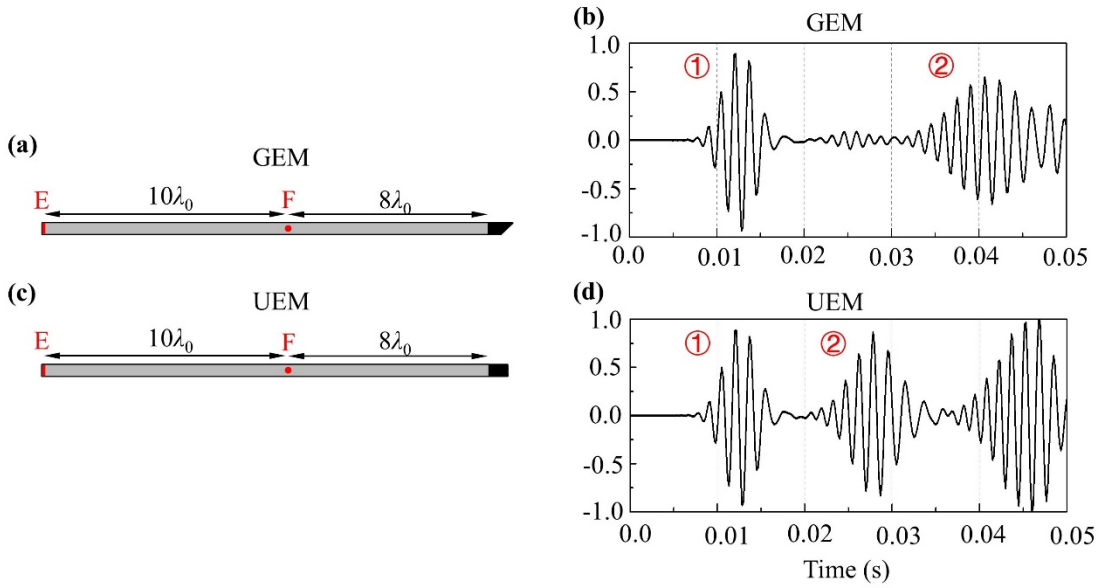
1 Fig. 6(b-ii). The LGEM realizes a high-efficiency and widen-angle absorption.
 2 Therefore, it is a perfect candidate for quasi-omnidirectional flexural wave absorption.
 3 To intuitively display the high-efficiency absorption, the incident wave with the
 4 incident angle of 0° is chosen to propagate into the GEM and LGEM, respectively. For
 5 these two cases, full reflected wave fields are solved analytically and numerically, as
 6 shown in Figs. 6(a-iii) and 6(b-iii). The results of full reflection wave fields are in good
 7 agreement with the reflection coefficients, which shows the reflection wave field almost
 8 disappears.



9
 10 FIG. 6 LGEM and GEM with surface phase gradient $\gamma=2.1k_0$. (a-i) and (b-i) The corresponding
 11 reflection angles of these diffraction modes for the GEM and LGEM, respectively. The color scale
 12 in (a-i) and (b-i) represent the value of reflection coefficient. (a-ii) and (b-ii) The reflection
 13 coefficients associated with each order propagation mode for the GEM and LGEM, respectively. (a-
 14 iii) and (b-iii) Analytical and numerical full reflection fields for the GEM and LGEM, respectively.

15 Further, for the quasi-omnidirectional LGEM, we intuitively show the multiple

1 reflections in the subunits by the analyses of the time domain signal. The computational
 2 model without considering loss is shown in Fig. 7(a). For comparison, the model of the
 3 lossless UEM is also shown in Fig. 7(c). The only difference between the two models
 4 is the subunit length, the one is gradient and the other is uniform. The periodic boundary
 5 conditions are applied to the two long boundaries of the models.



6
 7 FIG. 7 (a) The model of the supercell of GEM. (c) The model of the supercell of UEM. The signals
 8 over time received at the point F in (a) and (c) are shown in (b) and (d), respectively.

9 A 5-cycle tone burst signal $w_t = A_0 [1 - \cos(2\pi f_c t / 5)] \sin(2\pi f_c t)$ is applied on
 10 the line E, where $f_c = 600$ Hz is the central frequency. The point F, as shown in Figs.
 11 7(a) and 7(c), is the point of receiving signal. The corresponding received signals are
 12 shown in Figs. 7(b) and 7(d), where the signals ① and ② are the incident signal and
 13 reflection signal, respectively. It can be seen from Fig. 7(b) that the reflection signal for
 14 the GEM is delayed relative to that for the UEM in Fig. 7(d). It confirms that multiple
 15 reflections occur in the GEM.

5. Performance evaluation of the quasi-omnidirectional LGEM

To quantify the absorption performance of the quasi-omnidirectional LGEM, we examine the absorption coefficient varying with the frequency and incident angle by Eqs. (23) and (24). The corresponding results are shown in Fig. 8(a) with the white contour $\alpha=0.8$. The area of the high absorption coefficient, which is defined when the absorption coefficient exceeds 0.8, is located in the frequency range extending approximately from 340 Hz to 1000 Hz and for angles between -75° to 75° , except for the small area in the upper left corner in Fig. 8(a). Next, we will reveal the reasons for the low-efficiency absorption region in Fig. 8(a), including the region in the upper left corner, large incident angle region and low-frequency region.

5.1 The low-efficiency absorption induced by 1st order diffraction

In order to find out the reason of weak absorption in the upper left corner in Fig. 8(a), we calculate the reflection coefficients of the 0th order, -1th order, and 1st order diffraction varying with the frequency and incident angle, without considering the damping. The results are shown in Figs. 8(d), 8(e), and 8(f), respectively. It can be seen that the -1th order and 1st order diffractions dominate in the upper right and left corners in these figures, respectively, while the 0th order diffraction dominates in the rest of the region.

The reason is that when the frequency is greater than 660 Hz, the surface phase gradient γ will be less than $2k_0$. According to Eq. (20), the number of propagation modes increase to 3 for the incident angle range from -90° to 90° . In other words, another order propagation mode will exist in addition to the 0th order diffraction. The

1 added propagation modes are the -1^{th} order and 1^{st} order for the positive and negative
2 incident angle, respectively, according to Eq. (17). On the other hand, we know from
3 the above analysis that the 0^{th} order and -1^{th} order diffractions will be greatly absorbed
4 due to multiple reflections while the 1^{st} order diffraction cannot do due to only one
5 reflection. Therefore, in the upper left corner region of Fig. 8(a), the 1^{st} order diffraction
6 dominates and its low-efficiency absorption makes the value of absorption coefficient
7 very small.

8 *5.2 Impedance mismatch at the interface*

9 From Fig. 8(a), we can see that for the large incident angles ($>75^\circ$), the absorption
10 coefficient sharply drops. In order to reveal this phenomenon, we set up an analytical
11 model, as shown in the illustration of Fig. 8(b). The host plate and the waveguide
12 subunits, which are marked as Regions (1) and (2), respectively. The dotted line l_1 is
13 the interface between the two regions. The left and right ends of the model are the non-
14 reflection boundaries. The coefficient vectors in Regions (1) and (2) can be expressed
15 as $\hat{\mathbf{e}}_1 = \{\hat{A}_1, \hat{B}_1, \hat{C}_1, \hat{D}_1\}^T$ and $\hat{\mathbf{e}}_2 = \{\hat{A}_2, \hat{B}_2, \hat{C}_2, \hat{D}_2\}^T$. At the interface of l_1 ,
16 according to the boundary conditions, we can get $\hat{\mathbf{e}}_1 = \hat{T}_1 \hat{\mathbf{e}}_2$. Then, by deriving and
17 simplifying, we get $\{\hat{A}_2, \hat{C}_1\}^T = \hat{T}_2 \{\hat{A}_1, \hat{C}_2\}^T$, where \hat{T}_2 is the scattering matrix for a
18 reciprocal system, which already contains the information of the evanescent wave. On
19 the other hand, a general form of the 2×2 scattering matrix for a power-conserving and
20 reciprocal system can be expressed as (Liu et al., 2017b)

$$\hat{T}_2 = \begin{pmatrix} \frac{2\sqrt{Z}\sqrt{\eta}}{Z+1} & \frac{Z-1}{Z+1} \\ \frac{Z-1}{Z+1} & \frac{2\sqrt{Z}/\sqrt{\eta}}{Z+1} \end{pmatrix}, \quad (28)$$

where η has the physical meaning of power conservation. By comparing the two form of \hat{T}_2 , $p \approx l$, we can get the analytical impedance at the interface

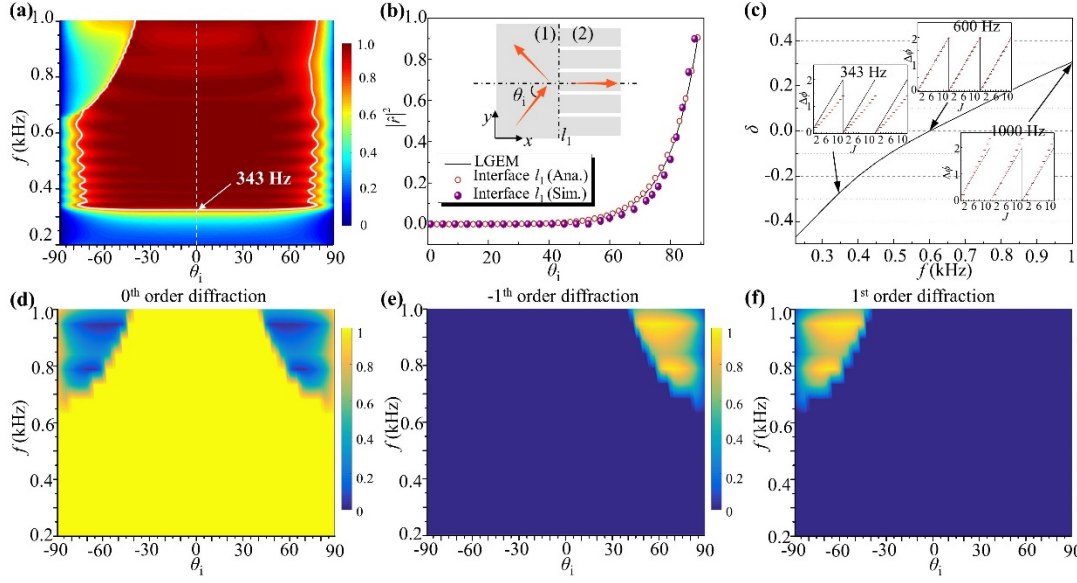
$$Z = \frac{2(\nu-1)k_0k_{y0}^2 + 4\nu k_0^3 + (\nu-1)^2k_{y0}^2\hat{k}_{x0}}{4\nu k_0^2k_{x0} - (\nu-1)^2k_{y0}^2k_{x0}}. \quad (29)$$

It can be seen from the above expression that the impedance at the interface is independent of the frequency. Based on Eq. (29), the reflection coefficient can be

obtained from $\hat{r} = \frac{Z-1}{Z+1}$ and expressed as

$$|\hat{r}| = \frac{2(\nu-1)k_0k_{y0}^2 + 4\nu k_0^2(k_0 - k_{x0}) + (\nu-1)^2k_{y0}^2(\hat{k}_{x0} + k_{x0})}{2(\nu-1)k_0k_{y0}^2 + 4\nu k_0^2(k_0 + k_{x0}) + (\nu-1)^2k_{y0}^2(\hat{k}_{x0} - k_{x0})}. \quad (30)$$

According to Eq. (30), the reflection coefficients induced by impedance mismatch at the interface l_1 are calculated and shown by the hollow circle line of Fig. 8(b). The corresponding simulated results are described by the solid circle line and in very good agreement with the analytical results. For comparison, the reflection coefficients of the LGEM in Fig. 6(b-ii) are added, as shown in the black solid line of Fig. 8(b). It can be seen that reflection coefficients for the LGEM are almost the same as that for the interface l_1 . This indicates that for the incident wave with a big incident angle ($>75^\circ$), the unabsorbed reflected wave from the LGEM is caused by the impedance mismatch at the interface between the host plate and the waveguide subunit. This is the reason that the absorptions coefficient sharply drops for the incident waves with very large incident angles.



1

2 FIG. 8 Performance evaluation of the LGEM. (a) The absorption coefficient varying with frequency
 3 and incident angle. For the reflection coefficients induced by impedance mismatch at the interface
 4 I_1 , the analytical and simulated results are the hollow circle line and solid circle line in (b),
 5 respectively. For comparison, the reflection coefficients of LGEM in Fig. 6(b-ii) is added to the
 6 black solid line of (b). (c) The change rate of phase shift for the supercell varying with the frequency.
 7 The phase shifts of all subunits for the frequencies of 343 Hz, 600 Hz, and 1000 Hz are shown in
 8 the illustration. (d), (e), and (f) are the reflection coefficients of 0th order, -1th order, and 1st order
 9 diffractions varying with the frequency and incident angle, respectively, without considering the
 10 damping.

11 5.3 Degenerated phase gradient in the low-frequency

12 It is worth noting that in Fig. 8(d) the 0th order diffraction dominates in the
 13 frequency range from 200 Hz to 650 Hz, but in Fig. 8(a) the absorption coefficient
 14 sharply drops in the range from 200 Hz to 343 Hz. In order to explain this phenomenon,
 15 the change rate of phase shift for the supercell varying with the frequency can be

1 defined as

$$2 \quad \delta(f) = \frac{\hat{\phi}(f) - \hat{\phi}_0}{\hat{\phi}_0}, \quad (31)$$

3 where $\hat{\phi}_0 = 2\pi$ is the phase shift for the supercell in the central frequency of 600 Hz.

4 The value of $|\delta|$ can quantify the degradation of the linear phase gradient. When $|\delta|$

5 is equal to 0, it shows that there is a perfect linear gradient. The more the value of $|\delta|$

6 is, the greater the degradation of the linear gradient is. According to Eqs. (15) and (31),

7 the value of δ varying with the frequency is shown in Fig. 8(c). It can be seen that

8 the change rate of δ has been less than -0.27 when the frequency is less than 343 Hz.

9 The phase shifts of all subunits for the frequencies of 343 Hz, 600 Hz, and 1000

10 Hz are shown in the illustrations of Fig. 8(c) as three typical examples. It can be seen

11 that phase shifts of all subunits decrease in the frequency of 343 Hz, in other words, the

12 linear phase gradient from the subunits has degenerated. It indicates that in the

13 frequency range below 343 Hz, the 0th order diffraction induced from the phase gradient

14 has been greatly generated by the decreased phase shift of the subunits, which will not

15 cause J -times reflections in the subunits. Therefore, the absorption coefficient sharply

16 drops in the range below 343 Hz. It should be pointed out that in Fig. 3(c) the loss of

17 the subunits has also some degeneration in the frequency range from 200 Hz to 343 Hz,

18 but the reduced loss has little effect on the absorption coefficient. In addition, the

19 degenerated phase gradient in the high frequency does not affect the 0th order diffraction,

20 which can result in high-efficiency absorption. The detailed explanation is shown in

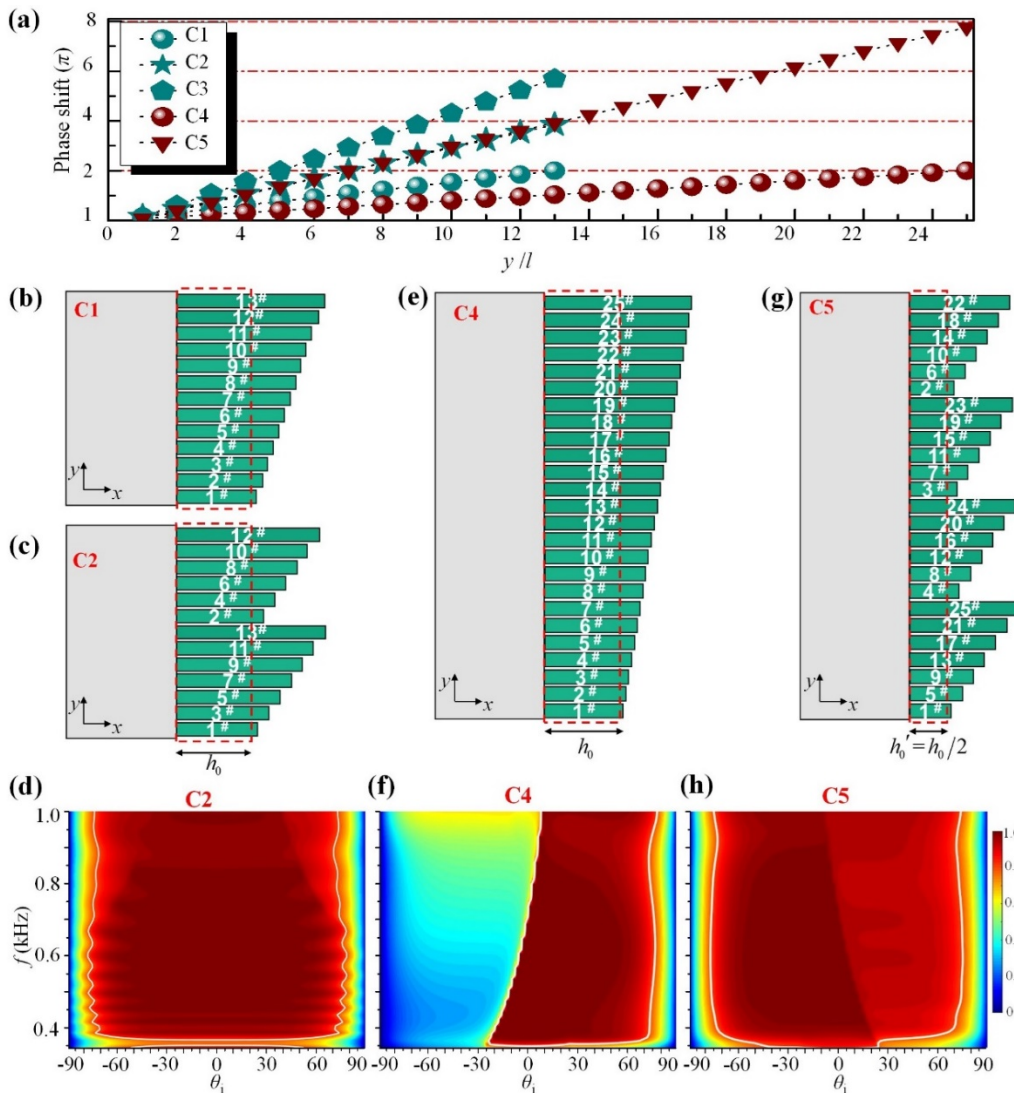
21 Appendix D.

6. Reducing the thickness of the quasi-omnidirectional LGEM

The above LGEM is designed in the central frequency of 600 Hz and its thickness (in the propagation direction) is determined by the maximum subunit length of $h_{12} = \lambda|_{f=600 \text{ Hz}}$ according to Eq. (5). When the frequency is less than 600 Hz, the designed thickness will be less than the wavelength. In other words, in the frequency range from 343 Hz to 600 Hz, high-efficiency absorption can be obtained by the LGEM with the sub-wavelength thickness, which is 0.76 times the maximum wavelength. In order to make the LGEM structure more compact in lower frequencies, we propose a general approach to further reduce its thickness while maintaining its high-efficiency absorption.

To understand, we first consider the supercell composed of 13 subunits, which is the 1st case marked as “C1”, shown in Fig. 9(a). The supercell has the same subunit width p and slit width p_0 as these of the above LGEM. All subunit lengths are redesigned to keep linear phase gradient by Eq. (5). According to Eq. (27), the time of multiple reflections for the 0th order diffraction is increased to 13 due to the subunit number is changed from 12 to 13. The corresponding absorption coefficient is almost the same as that in Fig. 8(a) due to the slightly increased reflection time. Further, we adjust the arrangement sequence of subunits in the supercell along y axis shown in Table 1, which is the 2nd case marked as “C2”. The corresponding model is shown in Fig. 9(b). The phase shift of each adjusted subunit along y axis is shown in Fig. 9(c). It can be found that the phase shift of the subunits for C2 still keeps linear changing due to the wave periodicity, but the phase shift of the supercell is doubled. This results in that the

1 phase gradient γ is doubled, compared to C1. According to Eq. (20), the number of
 2 propagation diffraction modes is reduced to 1 in the whole frequency range from 343
 3 Hz to 1000 Hz. It indicates that only the 0th order diffraction exists and the low-
 4 efficiency absorption induced by the 1st order diffraction is suppressed. The
 5 corresponding absorption coefficient is shown in Fig. 9(d). It can be seen that the low-
 6 efficiency absorption in the upper left corner shown in Fig. 8(a) disappears.



7
 8 FIG. 9 (a) Phase shift of each subunit for five cases along y axis. (b) The supercell of the 1st case is
 9 composed of 13 subunits and has the same subunit, slit widths, and phase gradient as these of the
 10 above LGEM. (c) The supercell of the 2nd case with the adjusted subunits. (e) The supercell of the

1 4th case with the additional length of h_0 . (g) The modified supercell of the 5th case with a short
2 additional length of h_0' . (d), (f), and (h) The absorption coefficient varying with the frequency and
3 incident angle for the 2nd, 4th, and 5th cases, respectively.

4 Table 1 The arrangement sequence of the subunits along y axis

	1	2	3	4	5	6	7	8	9	10	11	12	13	14	15
C ₁	1 [#]	2 [#]	3 [#]	4 [#]	5 [#]	6 [#]	7 [#]	8 [#]	9 [#]	10 [#]	11 [#]	12 [#]	13 [#]	/	/
C ₂	1 [#]	3 [#]	5 [#]	7 [#]	9 [#]	11 [#]	13 [#]	2 [#]	4 [#]	6 [#]	8 [#]	10 [#]	12 [#]	/	/
C ₃	1 [#]	4 [#]	7 [#]	10 [#]	13 [#]	3 [#]	6 [#]	9 [#]	12 [#]	2 [#]	5 [#]	8 [#]	11 [#]	/	/
C ₄	1 [#]	2 [#]	3 [#]	4 [#]	5 [#]	6 [#]	7 [#]	8 [#]	9 [#]	10 [#]	11 [#]	12 [#]	13 [#]	14 [#]	15 [#]
C ₅	1 [#]	5 [#]	9 [#]	13 [#]	17 [#]	21 [#]	25 [#]	4 [#]	8 [#]	12 [#]	16 [#]	20 [#]	24 [#]	3 [#]	7 [#]
	16	17	18	19	20	21	22	23	24	25	ζ		γ		
C ₁	/	/	/	/	/	/	/	/	/	/	$2\pi/13$		$2.1k_0$		
C ₂	/	/	/	/	/	/	/	/	/	/	$4\pi/13$		$4.2k_0$		
C ₃	/	/	/	/	/	/	/	/	/	/	$6\pi/13$		$6.3k_0$		
C ₄	16 [#]	17 [#]	18 [#]	19 [#]	20 [#]	21 [#]	22 [#]	23 [#]	24 [#]	25 [#]	$2\pi/25$		$1.05k_0$		
C ₅	11 [#]	15 [#]	19 [#]	23 [#]	2 [#]	6 [#]	10 [#]	14 [#]	18 [#]	22 [#]	$8\pi/25$		$4.2k_0$		

5
6 Based on the above analysis, by changing the arrangement sequence of the
7 subunits, the phase gradient can be increased by any positive integral multiple while
8 keeping linear due to the wave periodicity. For example, the arrangement sequence of
9 subunits is adjusted as the 3rd case, which is marked as “C3”. The corresponding
10 arrangement sequence and phase shift of subunits along y axis are shown in Table 1 and
11 Fig. 9(c), respectively. It can be found that the phase gradient of the C3 is increased by
12 3 times compared with that of C1, but the phase resolution ζ , which is $6\pi/13$ ($\approx \pi/2$),
13 is reduced by 3 times. From the corresponding calculating results, we get that
14 absorption coefficient of the C3 will be weakened in the high frequency of more than
15 700 Hz. This can be understood because good manipulation effect based phase requires
16 high phase resolution (Li et al., 2016). The low phase resolution weakens the multi-

1 reflection of the 0th diffraction mode. On the other hand, it should be pointed out that
2 for the supercells in which the number of subunits is even, the phase distribution will
3 have some small discontinuities after changing the arrangement sequence of the
4 subunits in the above way, but the effect can be ignored when the phase resolution is
5 much greater than $\pi/2$.

6 By the above three cases, we show that adjusting the arrangement sequence of
7 subunits in the supercell can suppress the 1st order propagation diffraction. Based on
8 this, we further show how to improve the supercell of the quasi-omnidirectional LGEM
9 with a small thickness while maintaining its high-efficiency absorption. The thickness
10 of LGEM with J subunits ($J=13$ in Fig. 9(a)), which has phase gradient of $\gamma > 2k_0$, is
11 determined by the maximum subunit length. The subunit length consists of two parts
12 according to Eq. (5). The first part is the length of $j\lambda_0/2J$, which produces linear
13 gradient distribution of phase. The second part is the additional fixed length of h_0 ,
14 which is mainly to enhance the absorption of multiple reflections. Here, we aim to
15 reduce the second part of the length. For reducing the first part, the corresponding detail
16 can be found in Appendix E.

17 For the improved supercell, the subunit number is increased by \hat{a} times, while
18 keeping subunit width, slit width, and additional fixed length unchanged. The subunit
19 lengths are redesigned to keep a linear gradient phase distribution according to Eq. (5).
20 For example, the number of subunits $J=13$ in Fig. 9(a) is increased to $J'=25$, which
21 is the 4th case marked C4, as shown in Fig. 9(e). The subunit number is increased by
22 $\hat{a} \approx 2$ times, but the phase gradient is reduced as $\gamma_4=1.05k_0$. According to Eq. (17),

1 the 1st order diffraction will dominate for the negative incident angle in the whole range
 2 from 343 Hz to 1000 Hz. This results in the low-efficiency absorption in this frequency
 3 range, the absorption coefficient of C4 is shown in Fig. 9(f).

4 Further, by adjusting the arrangement sequence of the above subunits, the phase
 5 shift of the supercell can be increased by \hat{b} times. The phase gradient and phase
 6 resolution of the above modified supercell can be rewritten as $\hat{\gamma}=\hat{b}\gamma/\hat{a}$ and ζ^*
 7 $=2\hat{b}\pi/\hat{a}J$, respectively. First, the modified phase gradient can satisfy the inequality of
 8 $\hat{\gamma} > \gamma$ to suppress low-efficiency absorption induced by the 1st order diffraction.
 9 Through the inequality, we can get the relation of $\hat{b} > \hat{a}$. Second, the modified phase
 10 resolution of ζ^* can be less than $\pi/2$ to ensure good diffraction performance. We can
 11 get the increased times \hat{b} as $\hat{b} < \hat{a}J/4$. Therefore, when \hat{b} fulfil the relation of

$$12 \quad \hat{a} < \hat{b} < \frac{\hat{a}J}{4}, \quad (\hat{a}, \hat{b} \in N^*), \quad (32)$$

13 the times of multiple reflections for 0th order diffraction mode is increased by \hat{a} times,
 14 without introducing other propagation diffraction modes. In this way, the absorption
 15 effect of the modified supercell will be increased by \hat{a} times according to Eq. (27).
 16 On the other hand, the additional fixed length of h_0 is reduced by \hat{a} times, the
 17 absorption effect from the additional length will be reduced by the same times.
 18 Therefore, when the additional fixed length of h_0 is reduced by \hat{a} times, at the same
 19 time, the multiple reflections is increased by \hat{a} times in the above way, the modified
 20 supercell can still keep the same high-efficiency absorption as the unmodified one in
 21 C1.

22 For example, the arrangement sequence of the subunits in C4 is redesigned, which

1 is the 5rd case marked as “C5”. When the subunit number is increased by $\hat{a} \approx 2$ times
 2 compared with C1, the phase gradient can be increased by $\hat{b} = 4$ times according to
 3 Eq. (32). In this way, the additional fixed length of h_0 can be reduced by $\hat{a} \approx 2$
 4 times while maintaining the same high-efficiency absorption. The modified supercell
 5 structure with the additional fixed length of $h_0' = h_0/2$ is shown in Fig. 9(g). The
 6 corresponding absorption coefficient is shown in Fig. 9(h). It can be found that in the
 7 frequency range from 343 Hz to 1000 Hz, the modified supercell can obtain the same
 8 high-efficiency absorption. Importantly, compared with the 1st case, the modified
 9 supercell thickness in propagation direction is less than the wavelength in the whole
 10 frequency range from 343 Hz to 1000 Hz and only 0.57 times the maximum wavelength.
 11 This confirms validity of the general approach, which can also be applied to the
 12 absorption of acoustic and electromagnetic wave metasurfaces. With these methods, we
 13 can further compress the thickness of the LGEM by a larger multiple to get a smaller
 14 or even deeper sub-wavelength thickness.

15 **7. Experiments of flexural waves absorption by the LGEM**

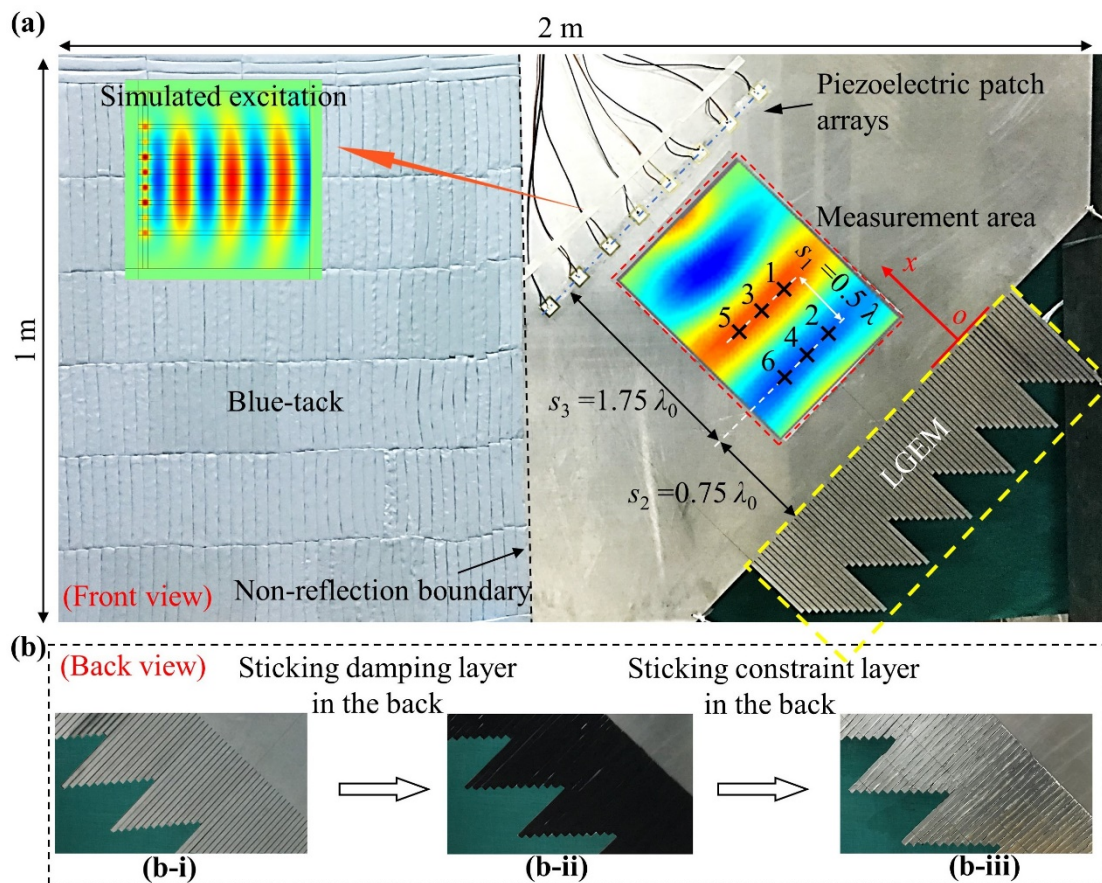
16 In order to further validate the vibrations absorption of the LGEM, we adopt the
 17 LGEM designed in the section 4.1 to perform a set of experimental investigations. The
 18 LGEM with phase gradient $\gamma = 2.1k_0$ is composed of twelve different subunits, as
 19 shown in Fig. 10(a). The fabrication process is shown in Fig. 10(b). First, the Wire
 20 Electrical Discharge Machining with a manufacturing precision of 0.05 mm is adopted
 21 to accurately fabricate the gradient strip-like aluminum plate by cutting a thin aluminum
 22 plate (2000 mm \times 1000 mm \times 3 mm). The back of the test piece is shown in Fig. 10(b-

1 i). Then, the damping layer (butyl rubber with a thickness of 3mm) is bonded on the
2 back of the strip-like aluminum plate, as shown in Fig. 10(b-ii). Finally, the constrained
3 layer (aluminum foil with a thickness of 0.15 mm) is bonded to the upper surface of the
4 damping layer as shown in Fig. 10(b-iii).

5 An array of eight piezoelectric patches ($20\text{ mm} \times 20\text{ mm} \times 0.3\text{ mm}$) with a distance
6 of 2.5λ from the LGEM is bonded on the surface of the plate as actuators. The LGEM
7 and the piezoelectric array are obliquely placed. In this way, the upward propagating
8 flexural wave excited by the piezoelectric patches is reflected by the upper boundary
9 into the left area attached with blue-tack (Liu et al., 2017b). The reflected flexural wave
10 will be fully absorbed in a large area of blue-tack. The boundary of blue-tack in the
11 middle of the plate can be equivalent to the non-reflection boundary, as shown in Fig.
12 10(a), which provides a reliable condition for the later steady-state experiments.

13 The built-in generator in the PSV-400 scanning laser Doppler vibrometer generates
14 a sinusoidal signal and transmit the signal to a power amplifier (HVPA05). The power
15 amplifier amplifies the signal and drives the eight piezoelectric patches. For the six
16 piezoelectric patches in the middle, the amplified voltage is two times of that for the
17 two outer piezoelectric patches. It should be pointed out that for different excitation
18 frequencies, one need to adjust the distance between piezoelectric patches to generate
19 a flexural wave Gaussian beam according to the phased array theory (Zhu et al., 2014b;
20 Cao et al., 2018c). For example, in the central frequency of 600 Hz, the distance
21 between piezoelectric plates is 2.5 times length of the piezoelectric patch width. Before
22 the experiment, we also use COMSOL Multiphysics 5.4 software (“Piezoelectric

1 Device” physic interface) to simulate the excited wave field. The corresponding
 2 simulated excitation wave field is shown in the upper left corner of Fig. 10(a). Before
 3 the absorption coefficient is tested, we scan the displacement field in the whole right
 4 part of plate, which has not blue-tack, through the PSV. The test results show that the
 5 intensity of the wave field in the measurement area is one order of magnitude larger
 6 than that in the other boundary within the test frequency range of 300 Hz to 1000 Hz.
 7 This indirectly proves the validity of the non-reflection boundary l_1 .



8
 9 FIG. 10 (a) The fabricated structure of the LGEM. The simulated excitation wave field is shown in
 10 the upper left corner. (b) The fabrication processes. The views are the back of the test piece in (a).

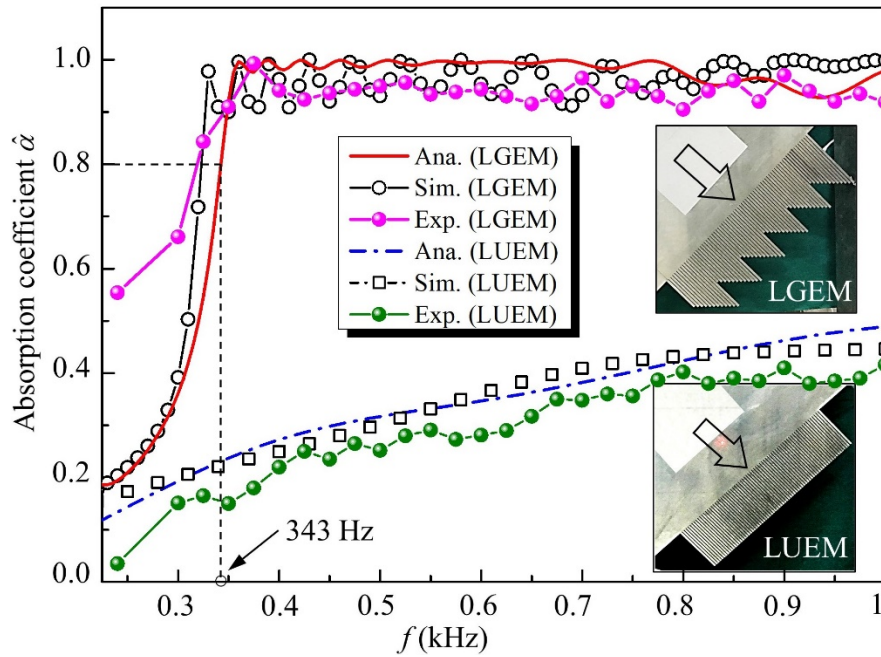
11 Six measurement points, marked in Fig. 10(a), are selected in the measurement
 12 area. These measurement points are divided into three groups: points 1 and 2, points 3

1 and 4, points 5 and 6. Their locations are marked in Fig. 10(a), which meets the far-
 2 field assumption (Denis et al., 2015). Therefore, the measurement wave field in these
 3 points can be well approximated as the sum of incident and reflection propagating
 4 waves. The out-of-plane complex displacements of these wave fields are measured by
 5 the laser scanning head of PSV-400 in the measurement mode of the frequency domain,
 6 which is perpendicularly aimed at the plate surface. An ensemble average with 50
 7 samples are used at every measurement point to ensure the signal quality.

8 First, for the points 1 and 2, we test the complex displacements, which can be
 9 expressed as $w^1 = W_1 \cdot e^{i(s_1+s_2) \cdot k} + W_R \cdot e^{-i(s_1+s_2) \cdot k}$ and $w^2 = W_1 e^{is_2 \cdot k} + W_R e^{-is_2 \cdot k}$,
 10 respectively. The transfer function H_{12} of the total wave field in the two points can be
 11 obtained from the measured complex displacements of w^1 and w^2 . It can be expressed
 12 as $H_{12} = w^2/w^1 = (e^{iks_2} + \tilde{r}e^{-iks_2}) / [e^{ik(s_1+s_2)} + \tilde{r}e^{-ik(s_1+s_2)}]$, where the reflection coefficient
 13 $\tilde{r} = W_R / W_1$. Then, we can calculate the reflection coefficient of
 14 $\tilde{r} = (H_{12} - e^{-iks_1}) \cdot e^{i2(s_1+s_2) \cdot k} / (e^{-iks_1} - H_{12})$ by the transfer function H_{12} , the distance s_1 ,
 15 s_2 , and the wavenumber k . Further, the experimental absorption coefficient can be
 16 obtained as $\hat{\alpha} = 1 - |\tilde{r}|^2$.

17 For the other two groups of measurement points, the absorption coefficient can
 18 also be obtained using the same method. Then, the average value of the three groups of
 19 measured absorption coefficients is the reliable reflection coefficient. These
 20 experimental results are shown in Fig. 11, which are in good agreement with both the
 21 theoretical and numerical simulation results. It shows that there is a high-efficiency
 22 absorption in the frequencies range approximately from 340 Hz to 1000 Hz. Some small

1 observed deviations come mainly from the manufacturing error of the specimen, the
 2 imperfect excitation signal and internal loss of the host plate. Especially, the large
 3 deviations in the low-frequency mainly come from the imperfect absorption of the blue-
 4 tack.



5
 6 FIG. 11 The absorption coefficients of the LGEM and the LUEM by experimental, analytical and
 7 simulation methods, respectively.

8 For comparison, the experiment of flexural wave absorption by the LUEM is also
 9 conducted. The test piece is illustrated in Fig. 11, and its back is bonded with
 10 constrained damping layer (not shown in the figure). It can be seen that the absorption
 11 coefficient is obviously smaller than that of the LGEM. The results are in good
 12 agreement with both theoretical and numerical simulation results. The comparison
 13 confirms that the gradient phase greatly enhances the absorption of flexural waves. In
 14 order to show the absorption effect intuitively, the dynamic full wave field for the
 15 central frequency of 600 Hz is obtained in measurement mode of the time domain, as

1 shown in Supplementary Video. It can be seen that the incident wave propagating in the
2 host plate is not superposed by the reflected wave from the boundary to form a standing
3 wave. It intuitively shows that the incident wave propagating to the boundary has been
4 efficiently absorbed by LGEM.

5 **8. Conclusions**

6 We have expanded the conventional mode-coupling method to analytically obtain
7 the full field reflection of each flexural wave diffraction mode, and revealed that the
8 flexural wave absorption behavior is due to multireflection-enhanced absorption of 0th
9 or -1th order diffractions. Further, we have introduced the concept of sub-wavelength
10 LGEM based on the 0th order diffraction to achieve a broadband and quasi-
11 omnidirectional absorption of flexural waves. We reveal that low-efficiency absorption
12 performance of the LGEM is mainly from the 1st order diffraction, the impedance
13 mismatch at the interface, and the degenerated gradient in the low-frequency. In
14 addition, the general approach of adjusting the arrangement sequence of subunits in the
15 supercell, which can eliminate low-efficiency absorption induced by the 1st order
16 diffraction, is proposed to further compress the thickness of the LGEM while
17 maintaining its high-efficiency absorption. Finally, the experiment confirms the high-
18 efficiency absorption of the LGEM in the frequencies range approximately from 340
19 Hz to 1000 Hz. This research could open up possibilities in the family of elastic
20 metamaterials and metasurfaces to realize broadband perfect absorption in low-
21 frequency by sub-wavelength structures.

1 **Acknowledgement**

2 This project is supported by the National Natural Science Foundation of China (Grant
3 No.11972296), the 111 Project (No. BP0719007), the Institute CARNOT (ICEEL), La
4 Région Grand Est, the Fundamental Research Funds for the Central Universities (No.
5 310201901A005). The first author is grateful to the support of Innovation Foundation
6 for Doctor Dissertation of Northwestern Polytechnical University (Grant No.
7 CX201936) and China Scholarship Council (CSC No. 201806290176).

8

1 **Appendix A. Detailed solution of the effective bending stiffness and wavenumber**
2 **of the lossy subunit**

3 The bending stiffnesses of the host plate, damping layer and constrained layer are

4 $D_0 = \frac{E_0 d_0^3}{12(1-\nu_0^2)}$, $D_{c1} = \frac{E_1 d_1^3}{12(1-\nu_1^2)}(1+i\cdot\eta)$, and $D_2 = \frac{E_2 d_2^3}{12(1-\nu_2^2)}$, respectively, where

5 E_1 is the real part of the complex Young modulus of the damping layer and E_2 is Young
6 modulus of the constraint layer. The tensile stiffnesses of the host plate, damping layer
7 and constrained layer are $K_0 = E_0 d_0 / (1-\nu_0^2)$, $K_{c1} = E_{c1} d_1 / (1-\nu_1^2)$, and
8 $K_2 = E_2 d_2 / (1-\nu_2^2)$, respectively. The effective bending stiffness of the lossy subunit

9 can be expressed as

10
$$D_{\text{eff}} = (D_0 + D_{c1} + D_2) + \left[K_0 d_c^2 + K_{c1} (d_{20} - d_c)^2 + K_2 (d_{30} - d_c)^2 \right] \\ - \left[K_{c1} \left(\frac{d_1}{12} + \frac{d_{20} - d_c}{2} \right) + K_2 (d_{30} - d_c) \right] \frac{d_{30} - d_c}{1 + g_c}, \quad (\text{A1})$$

11 where $d_c = \frac{K_{c1} \left(d_{20} - \frac{d_{30}}{2} \right) + (K_{c1} d_{20} + K_2 d_{30}) g_c}{K_0 + \frac{K_{c1}}{2} + (K_0 + K_{c1} + K_2) g_c}$ is the effective neutral-surface

12 position, $d_{20} = \frac{d_0 + d_1}{2}$, $d_{30} = \frac{d_0 + 2d_1 + d_2}{2}$, and $g_c = \frac{E_{c1}}{(1+\nu_1)K_2 d_1 k_{\text{eff}}^2}$. The effective

13 area density of the lossy subunit can be expressed as

14
$$m_{\text{eff}} = m_0 + m_1 + m_2, \quad (\text{A2})$$

15 where $m_0 = \rho_0 d_0$, $m_1 = \rho_1 d_1$, and $m_2 = \rho_2 d_2$ are the area density of the host plate,
16 damping layer and constrained layer, respectively. ρ_1 and ρ_2 are the material
17 density of the damping layer and constrained layer, respectively. The effective
18 wavenumber can be obtained by

$$k_{\text{eff}} = \left(m_{\text{eff}} \omega^2 / D_{\text{eff}} \right)^{1/4}. \quad (\text{A3})$$

According to Eqs. (A1)-(A3), we can calculate the effective wavenumber k_{eff} and effective bending stiffness D_{eff} .

Appendix B: The transfer matrixes between the state and coefficient vectors

$$T_1 = \begin{bmatrix} 1, 1, 1, 1 \\ -ik_0, ik_0, -k_0, k_0 \\ -D_0 k_0^2, -D_0 k_0^2, D_0 k_0^2, -D_0 k_0^2 \\ -iD_0 k_0^3, iD_0 k_0^3, D_0 k_0^3, -D_0 k_0^3 \end{bmatrix}, \quad (\text{B1})$$

$$T_2 = \begin{bmatrix} 1, 1, 1, 1 \\ -ik_{\text{eff}}, ik_{\text{eff}}, -k_{\text{eff}}, k_{\text{eff}} \\ -D_{\text{eff}} k_{\text{eff}}^2, -D_{\text{eff}} k_{\text{eff}}^2, D_{\text{eff}} k_{\text{eff}}^2, -D_{\text{eff}} k_{\text{eff}}^2 \\ -iD_{\text{eff}} k_{\text{eff}}^3, iD_{\text{eff}} k_{\text{eff}}^3, D_{\text{eff}} k_{\text{eff}}^3, -D_{\text{eff}} k_{\text{eff}}^3 \end{bmatrix}, \quad (\text{B2})$$

where T_1 and T_2 are the transformation matrix between the state vector and the coefficient vector for Regions (I) and (II) in the subunit, respectively. The matrix for the free boundary conditions T_4 is

$$T_4 = \begin{bmatrix} -D_{\text{eff}} k_{\text{eff}}^2 e^{-ik_{\text{eff}} h_j}, -D_{\text{eff}} k_{\text{eff}}^2 e^{ik_{\text{eff}} h_j}, D_{\text{eff}} k_{\text{eff}}^2 e^{-k_{\text{eff}} h_j}, -D_{\text{eff}} k_{\text{eff}}^2 e^{k_{\text{eff}} h_j} \\ -iD_{\text{eff}} k_{\text{eff}}^3 e^{-ik_{\text{eff}} h_j}, iD_{\text{eff}} k_{\text{eff}}^3 e^{ik_{\text{eff}} h_j}, D_{\text{eff}} k_{\text{eff}}^3 e^{-k_{\text{eff}} h_j}, -D_{\text{eff}} k_{\text{eff}}^3 e^{k_{\text{eff}} h_j} \end{bmatrix}. \quad (\text{B3})$$

Appendix C: Mode-coupling method for flexural waves diffraction modes

In x -axis direction shown in Fig. 1(a), the slope φ , bending moment M , and shear force V in the two-dimension plate model are rewritten as

$$\theta_x^{(p)} = \frac{\partial w^{(p)}}{\partial x}, \quad (\text{C1})$$

$$M_x^{(p)} = \begin{cases} D \left(\frac{\partial^2 w^{(p)}}{\partial x^2} + \nu \frac{\partial^2 w^{(p)}}{\partial y^2} \right) & y - y_j \leq |p/2| \\ 0 & y - y_j + p/2 \leq |(l-p)/2| \end{cases}, \quad (\text{C2})$$

$$V_x^{(p)} = \begin{cases} -D\left(\frac{\partial^3 w^{(p)}}{\partial x^3} + \frac{\partial^3 w^{(p)}}{\partial x \partial y^2}\right) & y - y_j \leq |p/2| \\ 0 & y - y_j + p/2 \leq |(l-p)/2| \end{cases}, \quad (C3)$$

where $y_j = (j-1)l$.

By applying the continuous boundary conditions of x -components of the displacement at the interface of $x=0$, and integrating with respect to y direction in the region $y - y_j \leq |p/2|$, we can get \square

$$\begin{pmatrix} {}_1P^1 \\ \vdots \\ {}_1P^j \\ \vdots \\ {}_1P^J \end{pmatrix} \mathbf{T}_i^p + \begin{pmatrix} {}_1\mathbf{H}_1^1 \cdots {}_1\mathbf{H}_n^1 \cdots {}_1\mathbf{H}_N^1 \\ \vdots \\ {}_1\mathbf{H}_1^j \cdots {}_1\mathbf{H}_n^j \cdots {}_1\mathbf{H}_N^j \\ \vdots \\ {}_1\mathbf{H}_1^J \cdots {}_1\mathbf{H}_n^J \cdots {}_1\mathbf{H}_N^J \end{pmatrix} \mathbf{T}_r^p = \begin{pmatrix} {}_1\mathbf{q}^1 & 0 & \cdots & \cdots & 0 \\ 0 & \ddots & 0 & \cdots & \vdots \\ \vdots & 0 & {}_1\mathbf{q}^j & 0 & \vdots \\ \vdots & \cdots & 0 & \ddots & 0 \\ 0 & \cdots & \cdots & 0 & {}_1\mathbf{q}^J \end{pmatrix} \mathbf{T}^s, \quad (C4)$$

where ${}_1\mathbf{H}_n^j(j, n) = [e^{-ik_{yn} \cdot y_j} \text{sinc}(k_{yn} \cdot p/2), e^{-ik_{yn} \cdot y_j} \text{sinc}(k_{yn} \cdot p/2)]$,

${}_1P^j(j) = e^{-ik_{y0} \cdot y_j} \text{sinc}(k_{y0} \cdot p/2)$, ${}_1\mathbf{q}^j = [1, 1, 1, 1]$. \mathbf{T}_i^p is the column vector whose elements are all A_i . Similarly, for the continuous boundary conditions of x -components

of the slop at the interface of $x=0$, we can get

$$\begin{pmatrix} {}_2P^1 \\ \vdots \\ {}_2P^j \\ \vdots \\ {}_2P^J \end{pmatrix} \mathbf{T}_i^p + \begin{pmatrix} {}_2\mathbf{H}_1^1 \cdots {}_2\mathbf{H}_n^1 \cdots {}_2\mathbf{H}_N^1 \\ \vdots \\ {}_2\mathbf{H}_1^j \cdots {}_2\mathbf{H}_n^j \cdots {}_2\mathbf{H}_N^j \\ \vdots \\ {}_2\mathbf{H}_1^J \cdots {}_2\mathbf{H}_n^J \cdots {}_2\mathbf{H}_N^J \end{pmatrix} \mathbf{T}_r^p = \begin{pmatrix} {}_2\mathbf{q}^1 & 0 & \cdots & \cdots & 0 \\ 0 & \ddots & 0 & \cdots & \vdots \\ \vdots & 0 & {}_2\mathbf{q}^j & 0 & \vdots \\ \vdots & \cdots & 0 & \ddots & 0 \\ 0 & \cdots & \cdots & 0 & {}_2\mathbf{q}^J \end{pmatrix} \mathbf{T}^s, \quad (C5)$$

where ${}_2P^j(j) = -ik_{x0} e^{-ik_{y0} \cdot y_j} \cdot \text{sinc}(k_{y0} \cdot p/2)$, ${}_2\mathbf{q}^j = [-ik_1, -k_1, ik_1, k_1]$,

${}_2\mathbf{H}_n^j(j, n) = [ik_{xn} e^{-ik_{yn} \cdot y_j} \cdot \text{sinc}(k_{yn} \cdot p/2), \bar{k}_{xn} e^{-ik_{yn} \cdot y_j} \cdot \text{sinc}(k_{yn} \cdot p/2)]$.

By applying the continuous boundary conditions of x -components of bending moment at the interface of $x=0$, and using the orthogonal relationship of the waveshapes and integrating with respect to y direction at the region $0 \leq y \leq g$, we can get

$$1 \quad \begin{pmatrix} {}_3P^1 \\ \vdots \\ {}_3P^n \\ \vdots \\ {}_3P^N \end{pmatrix} \mathbf{T}_i^P + \begin{pmatrix} {}_3\mathbf{H}_1 & 0 & \cdots & \cdots & 0 \\ 0 & \ddots & 0 & \cdots & \vdots \\ \vdots & 0 & {}_3\mathbf{H}_n & 0 & \vdots \\ \vdots & \cdots & 0 & \ddots & 0 \\ 0 & \cdots & \cdots & 0 & {}_3\mathbf{H}_N \end{pmatrix} \mathbf{T}_r^P = \begin{pmatrix} {}_3\mathbf{q}_1^1 \cdots & {}_3\mathbf{q}_1^j & \cdots & {}_3\mathbf{q}_1^J \\ \vdots & \vdots & & \vdots \\ {}_3\mathbf{q}_n^1 \cdots & {}_3\mathbf{q}_n^j & \cdots & {}_3\mathbf{q}_n^J \\ \vdots & \vdots & & \vdots \\ {}_3\mathbf{q}_N^1 \cdots & {}_3\mathbf{q}_N^j & \cdots & {}_3\mathbf{q}_N^J \end{pmatrix} \mathbf{T}^S, \quad (\text{C6})$$

2 where ${}_3\mathbf{q}_n^j(j, n) = [-\varsigma_1, \varsigma_1, -\varsigma_1, \varsigma_1]$, $\varsigma_1 = D_{\text{eff}} p k_1^2 \sin c(k_{yn} \cdot p / 2) \cdot e^{ik_{yn}y_j}$,
3 ${}_3P^n = D_0 L \cdot (-k_{x0}^2 - \nu k_{y0}^2)$, ${}_3\mathbf{H}_n(n) = [D_0 L \cdot (-k_{xn}^2 - \nu k_{yn}^2), \hat{k}_{xn}^2 - \nu k_{yn}^2]$. Similarly,
4 for the continuous boundary conditions of x -components of shear force at the interface
5 of $x=0$, we can get

$$6 \quad \begin{pmatrix} {}_4P^1 \\ \vdots \\ {}_4P^n \\ \vdots \\ {}_4P^N \end{pmatrix} \mathbf{T}_i^P + \begin{pmatrix} {}_4\mathbf{H}_1 & 0 & \cdots & \cdots & 0 \\ 0 & \ddots & 0 & \cdots & \vdots \\ \vdots & 0 & {}_4\mathbf{H}_n & 0 & \vdots \\ \vdots & \cdots & 0 & \ddots & 0 \\ 0 & \cdots & \cdots & 0 & {}_4\mathbf{H}_N \end{pmatrix} \mathbf{T}_r^P = \begin{pmatrix} {}_4\mathbf{q}_1^1 \cdots & {}_4\mathbf{q}_1^j & \cdots & {}_4\mathbf{q}_1^J \\ \vdots & \vdots & & \vdots \\ {}_4\mathbf{q}_n^1 \cdots & {}_4\mathbf{q}_n^j & \cdots & {}_4\mathbf{q}_n^J \\ \vdots & \vdots & & \vdots \\ {}_4\mathbf{q}_N^1 \cdots & {}_4\mathbf{q}_N^j & \cdots & {}_4\mathbf{q}_N^J \end{pmatrix} \mathbf{T}^S, \quad (\text{C7})$$

7 where ${}_4\mathbf{q}_n^j(j, n) = [i \cdot \varsigma_2, -\varsigma_2, -i \cdot \varsigma_2, \varsigma_2]$, $\varsigma_2 = D_{\text{eff}} p k_1^3 \sin c(k_{yn} \cdot p / 2) e^{ik_{yn}y_j}$,
8 ${}_4P^n = D_0 L \cdot (-ik_{x0}^3 - ik_{x0}k_{y0}^2)$, ${}_4\mathbf{H}_n(n) = D_0 L \cdot [(-ik_{xn}^3 - ik_{xn}k_{yn}^2), (\hat{k}_{xn}^3 - \hat{k}_{xn}k_{yn}^2)]$.

9 Since bending moment and shear forces are 0 at the right free boundary of the j^{th}
10 subunit, we can get

$$11 \quad \begin{pmatrix} {}_5\mathbf{I}^1 & 0 & \cdots & \cdots & 0 \\ 0 & \ddots & 0 & \cdots & \vdots \\ \vdots & 0 & {}_5\mathbf{I}^j & 0 & \vdots \\ \vdots & \cdots & 0 & \ddots & 0 \\ 0 & \cdots & \cdots & 0 & {}_5\mathbf{I}^J \end{pmatrix} \mathbf{T}^S = 0, \quad (\text{C8})$$

$$12 \quad \begin{pmatrix} {}_6\mathbf{I}^1 & 0 & \cdots & \cdots & 0 \\ 0 & \ddots & 0 & \cdots & \vdots \\ \vdots & 0 & {}_6\mathbf{I}^j & 0 & \vdots \\ \vdots & \cdots & 0 & \ddots & 0 \\ 0 & \cdots & \cdots & 0 & {}_6\mathbf{I}^J \end{pmatrix} \mathbf{T}^S = 0, \quad (\text{C9})$$

13 where ${}_5\mathbf{I}^j = (-e^{-ik_1h_j}, e^{-k_1h_j}, -e^{ik_1h_j}, e^{k_1h_j})$, ${}_6\mathbf{I}^j = (ie^{-ik_1h_j}, -e^{-k_1h_j}, -ie^{ik_1h_j}, e^{k_1h_j})$.

14 Eqs. (C4)-(C9), in turn, can be rewritten as

$$\begin{aligned}
& \mathbf{P}_1 \mathbf{T}_i^P + \mathbf{H}_1 \mathbf{T}_r^P = \mathbf{Q}_1 \mathbf{T}^S \\
& \mathbf{P}_2 \mathbf{T}_i^P + \mathbf{H}_2 \mathbf{T}_r^P = \mathbf{Q}_2 \mathbf{T}^S \\
& \mathbf{P}_3 \mathbf{T}_i^P + \mathbf{H}_3 \mathbf{T}_r^P = \mathbf{Q}_3 \mathbf{T}^S \\
& \mathbf{P}_4 \mathbf{T}_i^P + \mathbf{H}_4 \mathbf{T}_r^P = \mathbf{Q}_4 \mathbf{T}^S \\
& \mathbf{Q}_5 \mathbf{T}^S = \mathbf{0} \\
& \mathbf{Q}_6 \mathbf{T}^S = \mathbf{0}
\end{aligned} \tag{C10}$$

2 Finally, we can get

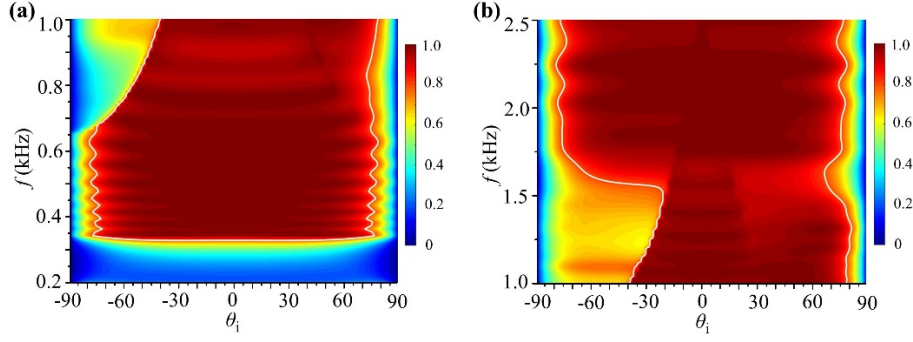
$$\mathbf{G}_1 \cdot \begin{pmatrix} \mathbf{T}_r^P \\ \mathbf{T}^S \end{pmatrix} = \mathbf{G}_2 \cdot \mathbf{T}_i^P, \tag{C11}$$

$$\text{where } \mathbf{G}_1 = \begin{pmatrix} -\mathbf{H}_1 & -\mathbf{H}_2 & -\mathbf{H}_3 & -\mathbf{H}_4 & \mathbf{0} & \mathbf{0} \\ \mathbf{Q}_1 & \mathbf{Q}_2 & \mathbf{Q}_3 & \mathbf{Q}_4 & \mathbf{Q}_5 & \mathbf{Q}_6 \end{pmatrix}^T, \mathbf{G}_2 = (\mathbf{P}_1 \ \mathbf{P}_2 \ \mathbf{P}_3 \ \mathbf{P}_4 \ 0 \ 0)^T.$$

6 **Appendix D: The influence of the degenerated phase gradient in the high** 7 **frequency and degenerated loss on the absorption**

8 It can be known from Fig. 3(c) that in the frequency range from 200 Hz to 343 Hz
9 the loss of the subunits has some degeneration. In order to find out whether the low-
10 efficiency absorption of LGEM ($\gamma=2.1k_0$) in low-frequency mainly comes from the
11 degenerated phase gradient or degenerated loss, we will fix the variable values of
12 storage modulus and loss factors for different frequencies to that in 600 Hz. In this way,
13 the non-degenerated loss is considered. The corresponding absorption coefficients
14 varying with the frequency and incident angle are shown in Fig. 12(a). Comparing Fig.
15 12(a) and Fig. 8(a), one can see that the absorption coefficients are almost the same. In
16 other words, the absorption effects are the same considering the degenerated loss and
17 non-degenerated one. This indicates that the low-efficiency absorption at low-
18 frequency mainly comes from the degenerated phase gradient rather than degenerated
19 loss.

1 On the other hand, it can be seen from Fig. 8(c) that the value of δ increases
2 with the frequency in the frequency range from 800 Hz to 1000 Hz. It means the linear
3 phase gradient has also degenerated in the high frequency. To clarify the effect of the
4 degenerated phase gradient in high frequency on the absorption, we study the
5 absorption coefficients in the frequency from 1000 Hz to 2500 Hz with considering
6 non-degenerated loss. The storage modulus and loss factors for different frequencies
7 are fixed to that in 600 Hz. The corresponding absorption coefficients is shown in Fig.
8 12(b). It can be found that there is a high-efficiency absorption in the whole frequency
9 range, except for the low-efficiency absorption in the lower left corner. The low-
10 efficiency absorption can be explained simply. The reason is that, in the frequency from
11 1000 Hz to 2500 Hz, three propagation diffraction modes, i.e., the -1^{th} , 0^{th} , and 1^{st} modes,
12 will exist. In the lower left corner of Fig. 12(b), the 1^{st} order diffraction dominates to
13 result in the low-efficiency absorption. The high-efficiency absorption in the remaining
14 region confirms that the degenerate phase gradient in high-frequency does not affect
15 the 0^{th} order diffraction. It should be pointed out that the degenerate phase gradient in
16 high-frequency is different from that in low-frequency. In the illustration of Fig. 8(c),
17 one can see the phase shift of the supercell for the frequency of 1000 Hz becomes bigger.
18 In other words, the phase shift of adjacent subunits still keeps a larger value in high
19 frequency, although the linear phase gradient has degenerated. This indicates that multi-
20 reflection induced by the 0^{th} order diffraction in high frequency is not very dependent
21 on linear phase shift.



1

2 Fig. 12 The absorption coefficient with considering non-degenerated loss in the frequency range (a)

3 from 200 Hz to 1000 Hz, (b) from 1000 Hz to 2500 Hz.

4 **Appendix E: Reducing the first part of the subunit length**

5 The wavelength of flexural waves can be calculated by

6
$$\lambda_0 = 2\pi \left(\frac{E_0 d_0^2}{12 \rho_0 \omega^2 (1 - \nu_0^2)} \right)^{1/4}$$
. Therefore, the first part of the subunit length $j\lambda_0/2J$

7 can also be reduced by changing the thickness of subunits $d_0' = \vartheta d_0$ in the direction of

8 z -axis, where ϑ is the thickness ratio. The performance of the subunit depends on the

9 matching degree of the impedance at the interface between the host plate and the

10 waveguide subunit. The better the impedance matching is, the smaller the reflection

11 coefficient at the interface is. It will result in a better performance. The reflection

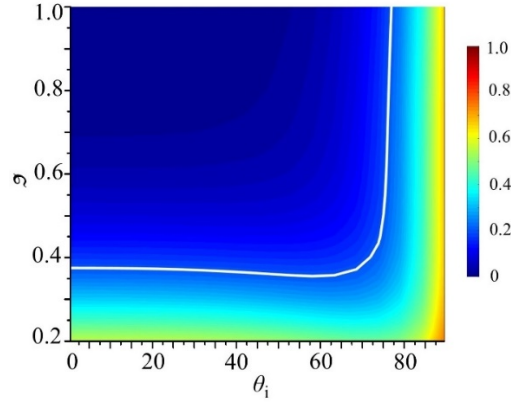
12 coefficients of incident power varying with the thickness ratio and incident angle are

13 shown in Fig. 13 with the white contour of 0.2. It can be found that changing the

14 thickness ratio in this range of $0.4 < \vartheta < 1$, the reflection coefficients are less than 0.2. This

15 means it is feasible to reduce the subunits length in this way. The aspects with more

16 detail will be the scope of future works.



1

2 Fig. 13 The reflection coefficients of incident wave varying with the thickness ratio and incident
 3 angle at the interface between the host plate and the waveguide subunit.

4 **Appendix F: Material parameters and simulation methods**

5 The host plate and constraint layer are made of aluminum alloy, with the elastic
 6 modulus $E_{\text{alu}} = 70 \text{ GPa}$, Poisson's ratio $\nu_{\text{alu}} = 0.33$, and the density
 7 $\rho_{\text{alu}} = 2700 \text{ kg/m}^3$. The complex elastic modulus of the damping layer can be obtained
 8 by Eq. (4). The density and Poisson's ratio of the damping layer are 1350 kg/m^3 and
 9 0.49, respectively. All the simulations are obtained using COMSOL Multiphysics 5.4
 10 software (Solid Mechanics Module). The periodic boundary conditions are applied to
 11 the two long boundaries of the strip-like structure in Region (I), as show in Fig. 1(b).
 12 PMLs are used on all outer boundaries to avoid any reflection from the boundaries. The
 13 full reflection wave fields in the Figs. 4 and 6 are obtained by subtracting the incident
 14 wave fields from the total wave fields in the post processing. The incident wave fields
 15 are obtained by the host plate without the LGEM or GEM structure.

16

1 **References**

- 2 Agnes, G., 1994. Active/passive piezoelectric vibration suppression. SPIE.
- 3 Assouar, B., Liang, B., Wu, Y., Li, Y., Cheng, J., Jing, Y., 2018. Acoustic metasurfaces. *Nat. Rev. Mater.*
4 3, 460-472.
- 5 Badreddine Assouar, M., Senesi, M., Oudich, M., Ruzzene, M., Hou, Z., 2012. Broadband plate-type
6 acoustic metamaterial for low-frequency sound attenuation. *Appl Phys Lett* 101, 173505.
- 7 Cao, L., Yang, Z., Xu, Y., Fan, S.-W., Zhu, Y., Chen, Z., Vincent, B., Assouar, B., 2020a. Disordered
8 Elastic Metasurfaces. *Phys. Rev. Appl.* 13, 014054.
- 9 Cao, L., Yang, Z., Xu, Y., Fan, S.-W., Zhu, Y., Chen, Z., Vincent, B., Assouar, B., 2020b. Disordered
10 elastic metasurfaces. *Phys. Rev. Appl.*
- 11 Cao, L.Y., Xu, Y.L., Assouar, B., Yang, Z.C., 2018a. Asymmetric flexural wave transmission based on
12 dual-layer elastic gradient. *Appl Phys Lett* 113, 183506.
- 13 Cao, L.Y., Yang, Z.C., Xu, Y.L., 2018b. Steering elastic SH waves in an anomalous way by metasurface.
14 *J. Sound Vib.* 418, 1-14.
- 15 Cao, L.Y., Yang, Z.C., Xu, Y.L., Assouar, B.M., 2018c. Deflecting flexural wave with high transmission
16 by using pillared elastic metasurface. *Smart Mater Struct* 27, 075051.
- 17 Chen, Y.Y., Li, X.P., Nassar, H., Hu, G.K., Huang, G.L., 2018. A programmable metasurface for real time
18 control of broadband elastic
19 rays. *Smart Mater Struct* 27, 115011.
- 20 Denis, V., Gautier, F., Pelat, A., Poittevin, J., 2015. Measurement and modelling of the reflection
21 coefficient of an Acoustic Black Hole termination. *J Sound Vib* 349, 67-79.
- 22 Dong, H.-W., Zhao, S.-D., Wang, Y.-S., Cheng, L., Zhang, C., 2020. Robust 2D/3D multi-polar acoustic

1 metamaterials with broadband double negativity. *J Mech Phys Solids*, 103889.

2 Dubay, R., Hassan, M., Li, C., Charest, M., 2014. Finite element based model predictive control for
3 active vibration suppression of a one-link flexible manipulator. *Isa T* 53, 1609-1619.

4 Fan, S.W., Zhao, S.D., Chen, A.L., Wang, Y.F., Assouar, B., Wang, Y.S., 2019. Tunable Broadband
5 Reflective Acoustic Metasurface. *Phys. Rev. Applied* 11, 044038.

6 Fang, X., Wen, J., Bonello, B., Yin, J., Yu, D., 2017. Ultra-low and ultra-broad-band nonlinear acoustic
7 metamaterials. *Nat Commun* 8, 1288.

8 Fu, Y., Shen, C., Cao, Y., Gao, L., Chen, H., Chan, C.T., Cummer, S.A., Xu, Y., 2019. Reversal of
9 transmission and reflection based on acoustic metagratings with integer parity design. *Nat Commun*
10 10, 2326.

11 Kerwin, E.M., 1959. Damping of Flexural Waves by a Constrained Viscoelastic Layer. *The Journal of*
12 *the Acoustical Society of America* 31, 952-962.

13 Krylov, V.V., Winward, R.E.T.B., 2007. Experimental investigation of the acoustic black hole effect for
14 flexural waves in tapered plates. *J Sound Vib* 300, 43-49.

15 Kweun, J.M., Lee, H.J., Oh, J.H., Seung, H.M., Kim, Y.Y., 2017. Transmodal Fabry-Perot Resonance:
16 Theory and Realization with Elastic Metamaterials. *Phys Rev Lett* 118.

17 Larouche, S., Smith, D.R., 2012. Reconciliation of generalized refraction with diffraction theory. *Opt*
18 *Lett* 37, 2391-2393.

19 Lee, H., Lee, J.K., Seung, H.M., Kim, Y.Y., 2018. Mass-stiffness substructuring of an elastic metasurface
20 for full transmission beam steering. *J. Mech. Phys. Solids* 112, 577-593.

21 Leng, J., Gautier, F., Pelat, A., Picó, R., Groby, J.P., Romero-García, V., 2019. Limits of flexural wave
22 absorption by open lossy resonators: reflection and transmission problems. *New J Phys* 21, 053003.

1 Li, S.L., Xu, J.W., Tang, J., 2018. Tunable modulation of refracted lamb wave front facilitated by adaptive
2 elastic metasurfaces. *Appl Phys Lett* 112, 021903.

3 Li, Y., Qi, S., Assouar, M.B., 2016. Theory of metascreen-based acoustic passive phased array. *New J Phys*
4 18, 1367-2630.

5 Li, Y., Shen, C., Xie, Y., Li, J., Wang, W., Cummer, S.A., Jing, Y., 2017. Tunable asymmetric transmission
6 via Lossy acoustic metasurfaces. *Phys Rev Lett* 119.

7 Liu, B., Jiang, Y., 2018. Metasurface-based angle-selective multichannel acoustic refractor. *Appl Phys*
8 *Express* 11, 057301.

9 Liu, B., Ren, B., Zhao, J., Xu, X., Feng, Y., Zhao, W., Jiang, Y., 2017a. Experimental realization of all-
10 angle negative refraction in acoustic gradient metasurface. *Appl Phys Lett* 111, 221602.

11 Liu, Y.Q., Liang, Z.X., Liu, F., Diba, O., Lamb, A., Li, J.S., 2017b. Source Illusion Devices for Flexural
12 Lamb Waves Using Elastic Metasurfaces. *Phys Rev Lett* 119, 034301.

13 Lustig, B., Elbaz, G., Muhafra, A., Shmuel, G., 2019. Anomalous energy transport in laminates with
14 exceptional points. *J Mech Phys Solids* 133.

15 Lustig, B., Shmuel, G., 2018. On the band gap universality of multiphase laminates and its applications.
16 *J Mech Phys Solids* 117, 37-53.

17 Ma, L., Cheng, L., 2019. Topological optimization of damping layout for minimized sound radiation of
18 an acoustic black hole plate. *J Sound Vib* 458, 349-364.

19 McCormick, C.A., Shepherd, M.R., 2019. Design optimization and performance comparison of three
20 styles of one-dimensional acoustic black hole vibration absorbers. *J Sound Vib*.

21 Mei, J., Wu, Y., 2014. Controllable transmission and total reflection through an impedance-matched
22 acoustic metasurface. *New J Phys* 16, 123007.

- 1 Moheimani, S.O.R., 2003. A survey of recent innovations in vibration damping and control using shunted
2 piezoelectric transducers. *IEEE T Contr Syst T* 11, 482-494.
- 3 Mokhtari, A.A., Lu, Y., Srivastava, A., 2019. On the properties of phononic eigenvalue problems. *J Mech*
4 *Phys Solids* 131, 167-179.
- 5 Mokhtari, A.A., Lu, Y., Zhou, Q., Amirkhizi, A.V., Srivastava, A., 2020. Scattering of in-plane elastic
6 waves at metamaterial interfaces. *Int J Eng Sci* 150.
- 7 Niederberger, D., Morari, M., 2006. An autonomous shunt circuit for vibration damping. *Smart Materials*
8 *and Structures* 15, 359-364.
- 9 Oudich, M., Li, Y., Assouar, B.M., Hou, Z., 2010. A sonic band gap based on the locally resonant
10 phononic plates with stubs. *New J Phys* 12, 083049.
- 11 Park, J., Lee, D., Rho, J., 2020. Recent Advances in Non-Traditional Elastic Wave Manipulation by
12 Macroscopic Artificial Structures. *Applied Sciences* 10.
- 13 Pelat, A., Gautier, F., Conlon, S.C., Semperlotti, F., 2020. The acoustic black hole: A review of theory
14 and applications. *J Sound Vib*.
- 15 Qi, S.B., Li, Y., Assouar, B.M., 2017. Acoustic Focusing and Energy Confinement Based on Multilateral
16 Metasurfaces. *Phys. Rev. Appl.* 7.
- 17 Qiu, H., Chen, M., Huan, Q., Li, F., 2019. Steering and focusing of fundamental shear horizontal guided
18 waves in plates by using multiple-strip metasurfaces. *EPL (Europhysics Letters)* 127, 46004.
- 19 Ross, D., Ungar, E.E., Kerwin, E.M., 1959. Damping of plate flexural vibration by means of viscoelastic
20 laminate. *Structural Damping*, ASME, New York.
- 21 Shen, C., Cummer, S.A., 2018. Harnessing Multiple Internal Reflections to Design Highly
22 Absorptive Acoustic Metasurfaces. *Phys. Rev. Appl.* 9, 054009.

- 1 Srivastava, A., 2016. Metamaterial properties of periodic laminates. *J Mech Phys Solids* 96, 252-263.
- 2 Su, X.S., Lu, Z.C., Norris, A.N., 2018. Elastic metasurfaces for splitting SV- and P-waves in elastic solids.
3 *J Appl Phys* 123, 091701.
- 4 Sugino, C., Ruzzene, M., Erturk, A., 2018. Merging mechanical and electromechanical bandgaps in
5 locally resonant metamaterials and metastructures. *J Mech Phys Solids* 116, 323-333.
- 6 Sun, J.Q., Jolly, M.R., Norris, M.A., 1995. Passive, Adaptive and Active Tuned Vibration Absorbers—A
7 Survey. *J Mech Design* 117, 234-242.
- 8 Tang, L., Cheng, L., Ji, H., Qiu, J., 2016. Characterization of acoustic black hole effect using a one-
9 dimensional fully-coupled and wavelet-decomposed semi-analytical model. *J Sound Vib* 374, 172-
10 184.
- 11 Tian, Z., Yu, L., 2019. Elastic Phased Diffraction Gratings for Manipulation of Ultrasonic Guided Waves
12 in Solids. *Phys. Rev. Appl.* 11, 024052.
- 13 Willis, J.R., 2016. Negative refraction in a laminate. *J Mech Phys Solids* 97, 10-18.
- 14 Xia, R., Yi, J., Chen, Z., Li, Z., 2019. In situ steering of shear horizontal waves in a plate by a tunable
15 electromechanical resonant elastic metasurface. *Journal of Physics D: Applied Physics* 53, 095302.
- 16 Xie, Y., Wang, W., Chen, H., Konneker, A., Popa, B.-I., Cummer, S.A., 2014. Wavefront modulation and
17 subwavelength diffractive acoustics with an acoustic metasurface. *Nat Commun* 5, 5553.
- 18 Xu, Y., Cao, L., Yang, Z., 2019a. Deflecting incident flexural waves by nonresonant singlephase meta-
19 slab with subunits of graded thicknesses. *J Sound Vib* 454, 51-62.
- 20 Xu, Y.L., Cao, L.Y., Yang, Z.C., 2019b. Deflecting incident flexural waves by nonresonant single-phase
21 meta-slab with subunits of graded thicknesses. *J Sound Vib* 454, 51-62.
- 22 Yi Fang, X.Z., Jie Zhou**, 2018. Acoustic porous metasurface for excellent sound absorption

1 based on wave manipulation.

2 Yu, N.F., Genevet, P., Kats, M.A., Aieta, F., Tetienne, J.P., Capasso, F., Gaburro, Z., 2011. Light
3 Propagation with Phase Discontinuities: Generalized Laws of Reflection and Refraction. *Science* 334,
4 333-337.

5 Yuan, S.-M., Chen, A.L., Wang, Y.-S., 2020. Switchable multifunctional fish-bone elastic metasurface
6 for transmitted plate wave modulation. *J Sound Vib* 470, 115168.

7 Zhang, H.K., Chen, Y., Liu, X.N., Hu, G.K., 2020. An asymmetric elastic metamaterial model for elastic
8 wave cloaking. *J Mech Phys Solids* 135, 103796.

9 Zhang, J., Su, X., Liu, Y.L., Zhao, Y.X., Jing, X., Hu, N., 2018. Metasurface constituted by thin composite
10 beams to steer flexural waves in thin plates. *Int. J. Solids Struct.* 162, 14-20.

11 Zhilin Hou, * Xinsheng Fang,2 Yong Li ,2,† and Badreddine Assouar 3, 2019. Highly Efficient Acoustic
12 Metagrating with Strongly Coupled Surface Grooves. *Phys. Rev. Appl.*

13 Zhou, J., Zhang, X., Fang, Y., 2017. Three-dimensional acoustic characteristic study of porous
14 metasurface. *Compos Struct* 176, 1005-1012.

15 Zhu, H., Semperlotti, F., 2016. Anomalous Refraction of Acoustic Guided Waves in Solids with
16 Geometrically Tapered Metasurfaces. *Phys Rev Lett* 117, 034302.

17 Zhu, H.F., Walsh, T.F., Semperlotti, F., 2018a. Total-internal-reflection elastic metasurfaces: design and
18 application to structural vibration isolation. *Appl Phys Lett* 113,, 221903.

19 Zhu, R., Liu, X.N., Hu, G.K., Sun, C.T., Huang, G.L., 2014a. A chiral elastic metamaterial beam for
20 broadband vibration suppression. *J Sound Vib* 333, 2759-2773.

21 Zhu, R., Liu, X.N., Hu, G.K., Sun, C.T., Huang, G.L., 2014b. Negative refraction of elastic waves at the
22 deep-subwavelength scale in a single-phase metamaterial. *Nat. Commun.* 5, 5510.

1 Zhu, Y., Hu, J., Fan, X., Yang, J., Liang, B., Zhu, X., Cheng, J., 2018b. Fine manipulation of sound via
2 lossy metamaterials with independent and arbitrary reflection amplitude and phase. *Nat. Commun.* 9,
3 1632.
4